

UDK 553.492:550.837.3:518.5=20

Indirect geophysical model of Istrian bauxite deposits

Janez Lapajne

Geološki zavod, 61000 Ljubljana, Parmova 33

Abstract

The bauxite bodies in Istria lie rather deep and are too small to be directly identified. Bauxite is a common residual constituent found in pockets of Cretaceous limestone. During its formation and compaction, its volume is reduced. Therefore its hanging wall, consisting of Eocene limestone, settles in the Cretaceous pocket. The rents and fissures in the hanging wall are filled with clay. Due to favorable wet conditions this geological structure becomes a low resistivity body, corresponding to a hemispheroid or dike. Resistivity curves over these models fit the corresponding observed resistivity profiles very well, the difference being within a few percent on average. The paper contains a collection of resistivity type curves. With regard to the hemispheroid, there occurs in specific conditions a remarkable paradox: the thinner the hemispheroid, the more significant the anomaly.

Kratka vsebina

Boksitna telesa leže v Istri pregloboko in so premajhna, da bi jih mogli najti z direktnimi raziskovalnimi metodami. Geološke razmere v njihovih nahajališčih pa so ugodne za uporabo indirektnih metod. Kot preostanek preperevanja krednega apnenca se je boksit zbral v žepih krednih plasti, ki jih je prekril eocenski apnenec. Ker se je med nastajanjem boksita njegova prostornina zmanjševala, se je začela posedati njegova krovina iz eocenskega apnenca. Med posedanjem so eocenske plasti razpokale in razpoke je zapolnila glina. Na ta način so nastale ugodne razmere za povečanje vlažnosti v krednem žepu, ki je postal nizkouporno telo. Tej geološki strukturi ustreza model polsferoida, v določenem primeru pa model plošče. Teoretične krivulje modelov se razlikujejo od ustreznih izmerjenih vrednosti poprečno le za nekaj odstotkov. Poleg kvalitativnega in kvantitativnega vrednotenja upornostnih anomalij boksitnih žepov vsebuje članek večji izbor modelnih krivulj. Pri polsferoidu se je pokazal zanimiv paradoks: Čim tanjši je polsferoid, tem večjo anomalijo povzroča.

Contents

1. The resistivity anomalies of bauxite deposits in Istria	128
1.1. Introduction	128
1.2. The direct and indirect approach	128
1.3. Test resistivity survey	131
1.4. Detailed resistivity profiling	131
1.5. Results of core drilling	136

2. Mathematical modelling	137
2.1. Basic equations	137
2.2. Resistivity type curves	142
2.3. Analysis of resistivity type curves	167
3. The quantitative processing of anomalies	170
3.1. Numerical proceedings	170
3.2. Results of quantitative processing	173
3.3. Discussion	187
4. Conclusions	187
References	188

1. The resistivity anomalies of bauxite deposits in Istria

1.1. Introduction

The subsurface conditions in bauxite deposits at Karojba in Istria were explored in 1966. Geological mapping was immediately followed by a geophysical survey and subsequently by core drilling. It was already known that bauxite occurs in Cretaceous limestone pockets. Its hanging wall is of Eocene limestone, which overlies the Cretaceous limestone to the North of the line Umag—Labin, whereas proceeding southwards of this geological boundary, Eocene erosion remnants are to be found (fig. 1).

1.2. The direct and indirect approach

The differences in physical parameters between a buried body and its surrounding rock may cause geophysical anomalies, measurable on the surface. In this case, the buried body is discovered directly. With regard to the known physical parameters, it is relatively easy to estimate the depth and the dimension of the bodies of simple geometrical forms, by applying the iterative numerical method, provided the body and its country rock are homogenous units. However, results of laboratory and mathematic model investigations clearly show that the direct approach is suitable for shallow geological conditions. The Wenner array, with electrodes separated at a suitable distance, registers a change of approximately only 10 per cent of apparent resistivity when a perfectly conducting sphere lies at a depth (distance from the surface to the center of the sphere) which equals the diameter of the body. Applicable variations of this measured parameter must conform to following equation:

$$\frac{\Delta V}{V} > 2 p_r$$

V = measured quantity,

ΔV = change in the measured quantity,

p_r = relative error of measurement.

In the case of resistivity surveys, the error of measurement is considered to be as much as 5 per cent. Due to the influence of topography and the inhomogeneity of the field, the change in measured quantity for even 10 per cent can hardly be recognized.

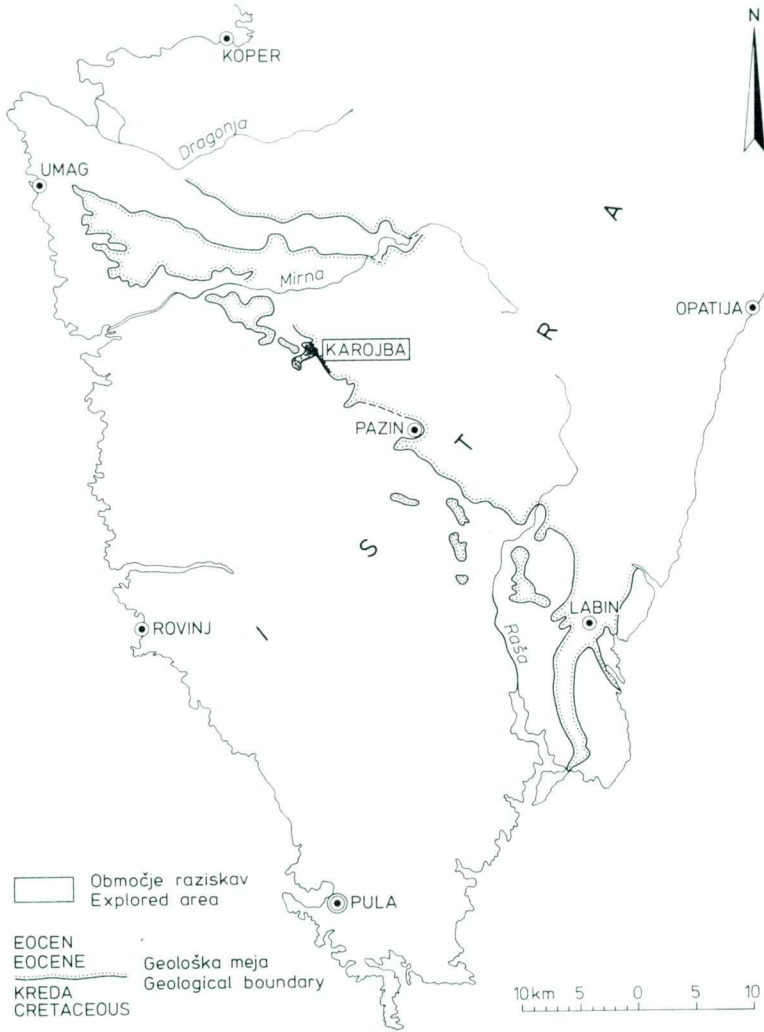


Fig. 1. Location map of explored bauxite deposits at Karojba (After J. Lapajne, 1969)

Sl. 1. Situacija raziskanih boksitnih nahajališč pri Karojbi (Po J. Lapajne, 1969)

Fortunately, geological and hydrogeological conditions may make it possible to prospect a buried body indirectly, resulting from the resistivity properties of its cover. This possibility must be studied on natural models in well known geological conditions resembling the potential investigation area. By means of indirect investigation and an appropriate interpretation process, it is possible to obtain the required geological information.

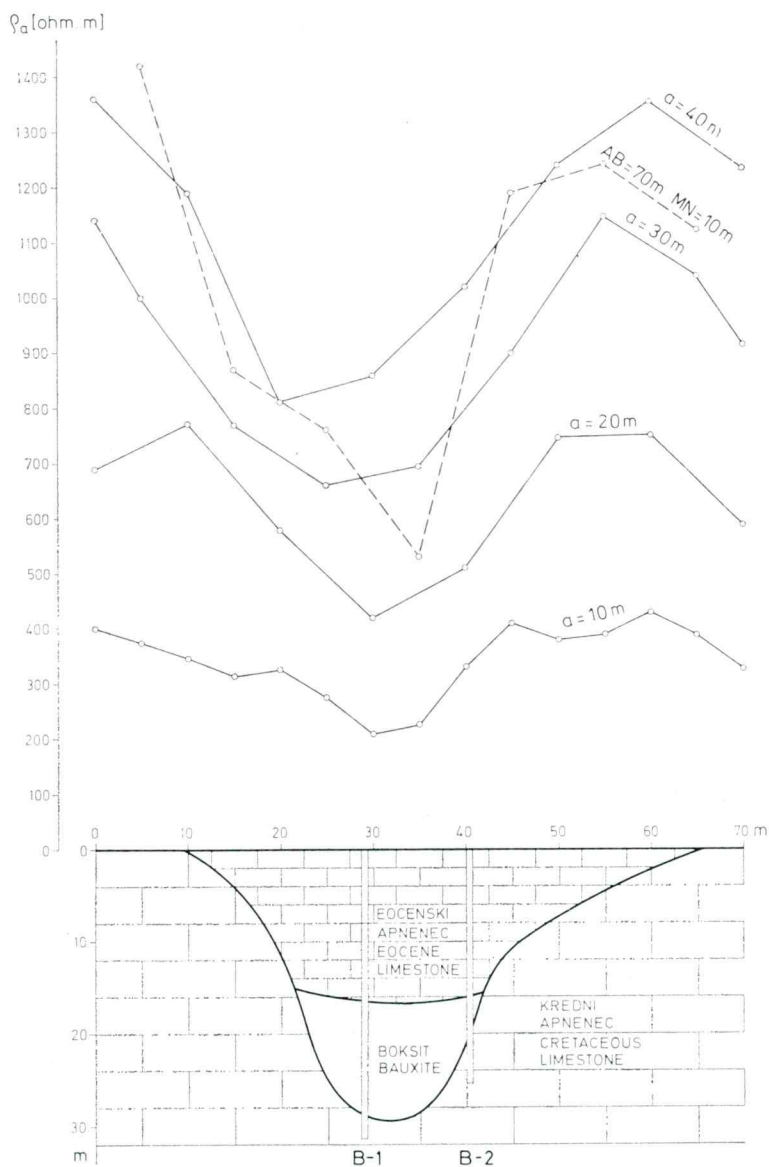


Fig. 2. Observed resistivity profiles on the erosion remnant of Eocene limestone (test location)

Sl. 2. Profili navidezne specifične upornosti na krpi eocenskega apnenca (poskusna lokacija)

1.3. Test resistivity survey

Test measurements have been carried out in a selected area, the geological setting of which has been controlled by drilling. The Eocene beds overlying the bauxite body are somewhat thicker than elsewhere, a fact which by itself cannot serve as an explanation for existing anomalies, as no essential difference is to be found between the electrical resistivity of the Eocene and Cretaceous limestones. The resistivity values obtained are as follows:

Cretaceous and Eocene limestone	1000—3000 ohm.m
bauxite	100—300 ohm.m
clay, humus, terra rossa, marl, water	10—100 ohm.m

(Note: Some of the values were not within the limits given above.)

The indirect relationship of the anomaly to the bauxite can be interpreted in terms of the origins of the bauxite. The formation of bauxite is related to a volumetric shrinkage, which causes a gradual sinking of the bauxite hanging wall. Consequently, moderate depressions in places clearly indicate distinctive superficial features marking the Cretaceous bauxite pockets. Cracks, rents and fissures filled with clay traverse the sunken Eocene calcareous hanging wall, thereby causing favourable wet ground conditions. That is why the bauxite pockets appear as low resistivity bodies. Hemispheroids and dikes may accordingly represent the models of such structures (figs. 2—7).

Taking into consideration the geological features, the prolate hemispheroid seems to be the most appropriate for evaluation. The model curves already published for hemispheres (K. L. Cook and R. L. Gray, 1961) and vertical dikes, as well as one for oblate hemispheroids (K. L. Cook and R. G. Van Nostrand, 1954), together with field measurement, show that the anomalies may likewise be explained by these models. This means that the deviation in geophysical quantities observed at the Istrian bauxite deposits, originates mainly in the hanging wall of Eocene itself. Fig. 8 shows a geological profile of the test locality (b) and suggested geoelectrical models (a).

1.4. Detailed resistivity profiling

On the basis of all the previous geological and geophysical information, an area has been prospected 1.5 sq km North of the Cretaceous/Eocene limestone boundary. Taking previous resistivity investigations into consideration, only one array dimension seemed to be appropriate for resistivity profiling, as in the case of a larger number of electrode separations, the work would be time consuming and would increase costs.

At the beginning, measurements were carried out by the Wenner array, where electrode spacing equalled 10 m, 20 m, 30 m and 40 m. Experience had suggested that an array of 30 m would be the most appropriate both in the field survey and in interpretation. In certain sections additional data were gathered by varying the separation of electrodes. The survey was carried out in roughly parallel lines, the separation of electrodes being 30 m and the distance of adjacent observation points reaching 10 m. The length of all survey lines totalled 63 km.

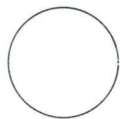
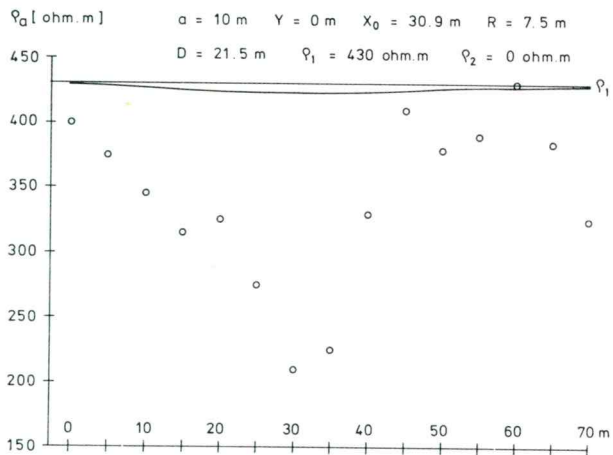


Fig. 3. Test location. Observed resistivity profile over bauxite deposit and theoretical plot over direct model — buried conducting sphere. Wenner array, $a = 10 \text{ m}$

Sl. 3. Poskusna lokacija. Teoretična krivulja neposrednega modela — prevodne krogle v homogenem polprostoru in merske vrednosti Wennerjeva razvrstitev, $a = 10 \text{ m}$

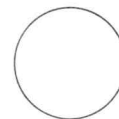
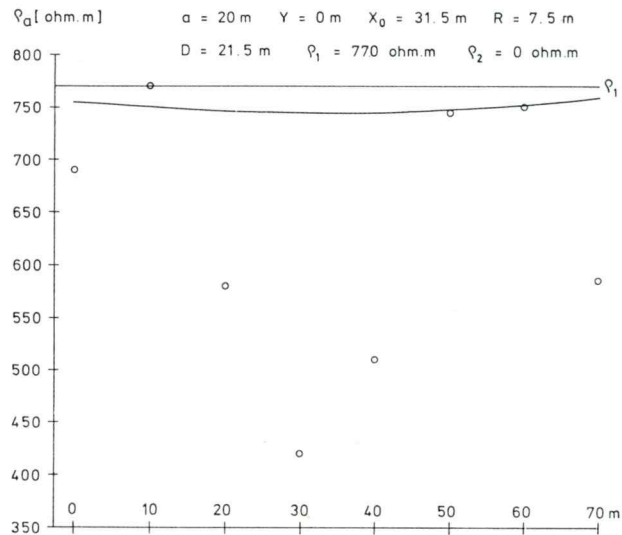


Fig. 4. Test location. Observed resistivity profile over bauxite deposit and theoretical plot over direct model — buried conducting sphere. Wenner array, $a = 20 \text{ m}$

Sl. 4. Poskusna lokacija. Teoretična krivulja neposrednega modela — prevodne krogle v homogenem polprostoru in merske vrednosti Wennerjeva razvrstitev, $a = 20 \text{ m}$

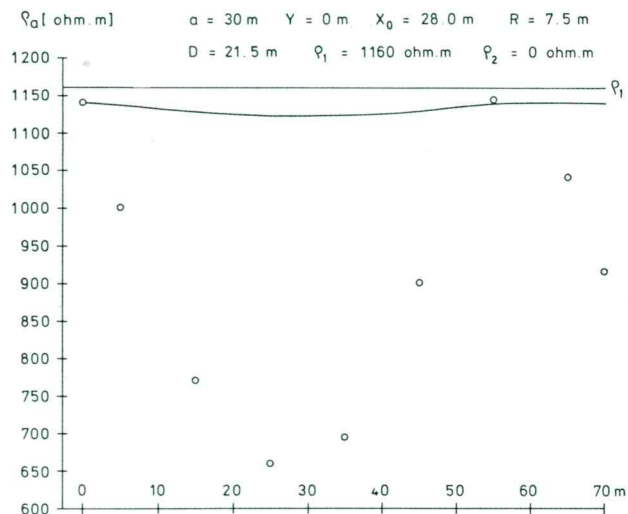


Fig. 5. Test location. Observed resistivity profile over bauxite deposit and theoretical plot over direct model — buried conducting sphere. Wenner array, $a = 30 \text{ m}$

Sl. 5. Poskusna lokacija. Teoretična krivulja neposrednega modela — prevodne krogle v homogenem polprostoru in merske vrednosti. Wennerjeva razvrstitev, $a = 30 \text{ m}$

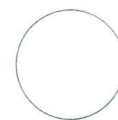
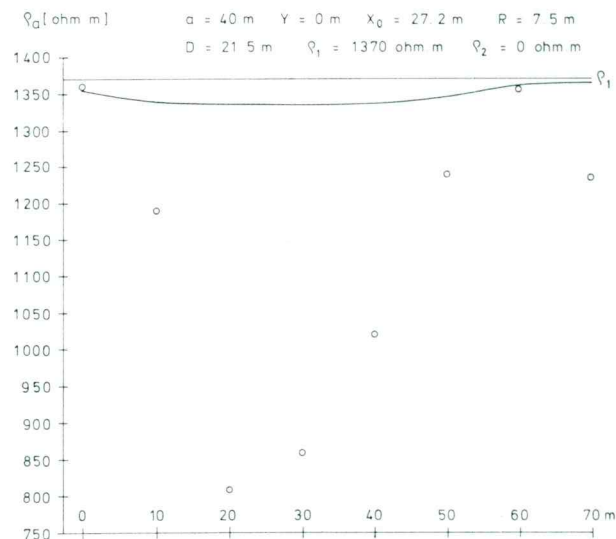


Fig. 6. Test location. Observed resistivity profile over bauxite deposit and theoretical plot over direct model — buried conducting sphere. Wenner array, $a = 40 \text{ m}$

Sl. 6. Poskusna lokacija. Teoretična krivulja neposrednega modela — prevodne krogle v homogenem polprostoru in merske vrednosti. Wennerjeva razvrstitev, $a = 40 \text{ m}$

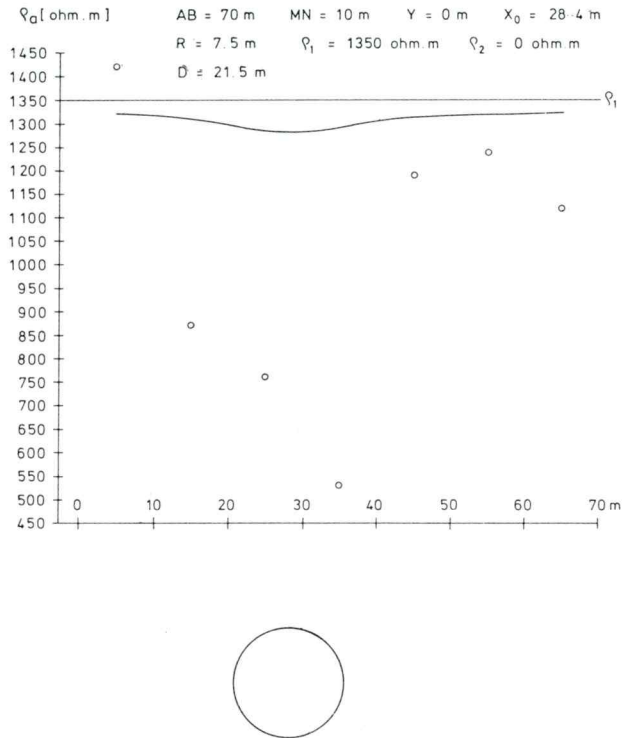


Fig. 7. Test location, Observed resistivity profile over bauxite deposit and theoretical plot over direct model — buried conducting sphere. Schlumberger array, MN = 10 m and AB = 70 m

Sl. 7. Poskusna lokacija. Teoretična krivulja neposrednega modela — prevodne krogle v homogenem polprostoru in merske vrednosti. Schlumbergerjeva razvrstitev, MN = 10 m in AB = 70 m

Although the accepted explanation of the origin of resistivity anomalies seems reasonable, the interpretation of detailed investigations proved to be extremely difficult. The ambiguities in interpretation are best evident in the apparent resistivity profile measured in the field (fig. 9), which features a number of anomalies, of which only one has proved to be positive. Resistivity profiles were found to be similar in both rock units. Since there is no significant difference in resistivity between the Eocene and Cretaceous limestones, it is not possible to recognize their geological boundaries.

A satisfactory interpretation could have been achieved by the careful comparison of geological and geophysical data. The geology was plotted on survey lines in order to perceive the anomalies occurring on Eocene limestone. Anomalies could have been affected by the inhomogeneity of the surface, which has no relation whatsoever with bauxite deposits. Such inhomogeneities are for instance sinkholes filled with clayey residue.

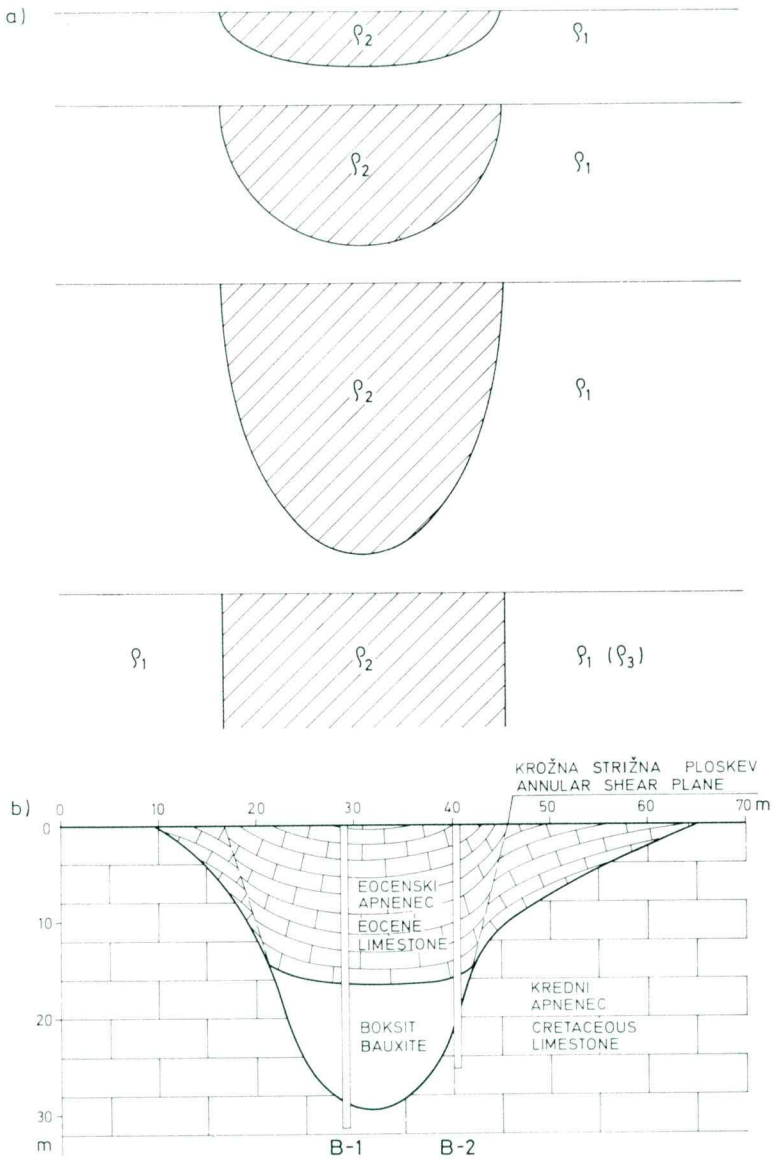


Fig. 8. Models explaining resistivity anomalies over bauxite deposits in Istria (a) and test location cross section (b)

Sl. 8. Modeli, ki lahko pojasnijo geoelektrične anomalije istrskih boksitnih nahajališč (a) in geološki prerez poskusne lokacije (b)

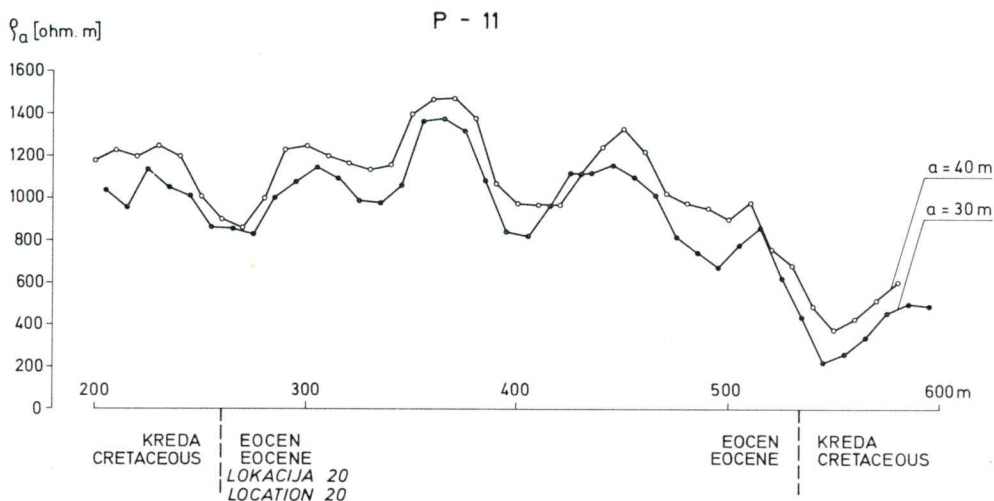


Fig. 9. Observed horizontal resistivity profile from the explored area
 Sl. 9. Profil navidezne specifične električne upornosti z raziskovalnega območja

It is comparatively easy to eliminate the corresponding anomalies. Additional visible inhomogeneities consist of troughs of residue accumulated on uneven calcareous ground. The depth of terra rossa and clay in minor sinkholes was established by the hand drill, which, unfortunately, could not penetrate more than two meters. Observation of the bedding provided additional, useful geological information. Centrally-inclined beds of Eocene limestone indicated circular settlements and it was under such structures that bauxite deposits could be expected.

All the anomalies concerning the topographic influences and sinkholes in which terra rossa lay two meters thick or more, were eliminated. Therefore, it is quite possible that some useful anomalies were lost. However, taking into consideration the fact that each anomaly could not have been controlled by drilling, then this procedure was correct, as some hundred anomalies occurred. Where necessary, additional measurements on parallel or cross survey lines were carried out.

1.5. Results of core drilling

The geophysical survey enabled the selection of 75 drilling sites, the majority of which exhibit the centrally-inclined position of the Eocene beds. On the other hand, 13 sites where no resistivity anomalies were found were deemed appropriate for testing in depth on geological grounds only.

From 75 drilling sites located in consideration of their geological + geophysical positions, 19 penetrated bauxite and 39 clay, whereas 17 locations were found to be negative. The examination of drillcores proved a subsidence of beds. All 13 drilling sites located on merely geological grounds proved to be negative.

2. Mathematical modelling

2.1. Basic equations

The simplest model of pocket bauxite body in Istria is the sphere in half-space of infinite extent (fig. 10). At a depth exceeding the radius of the sphere, the potential of the point-source current is given by B. K. Matveev (1961) corrected by coefficient 2 introduced within the equation (1-1). The corresponding quantities determine the equations (1-a).

It has been shown in the previous chapter that the direct model is not suitable for interpreting the observed anomalies. The indirect model of filled-sink is therefore applied as for the hemiellipsoid. For plate-like hanging wall depressions, the hemiellipsoid of revolution — hemispheroid (fig. 11) — appears to be a suitable model for a pocket-like bauxite deposit.

The point-source potential is thus given by:

equations (2-1) up to (2-4) for hemispheres

equations (4-1) up to (4-4) for prolate hemispheroids

equations (5-1) up to (5-4) for oblate hemispheroids.

The first subscript denotes the observation point, and the second subscript denotes the current source. Subindex "1" denotes the country rock, and subindex "2" indicates the model body. The meaning of the symbols is evident in fig. 11 and in the equations (2-a), (4-a) and (5-a). Equations (2-1) up to (2-4), (4-1) up to (4-4), and (5-1) up to (5-4) are taken from K. L. Cook & R. G. Van

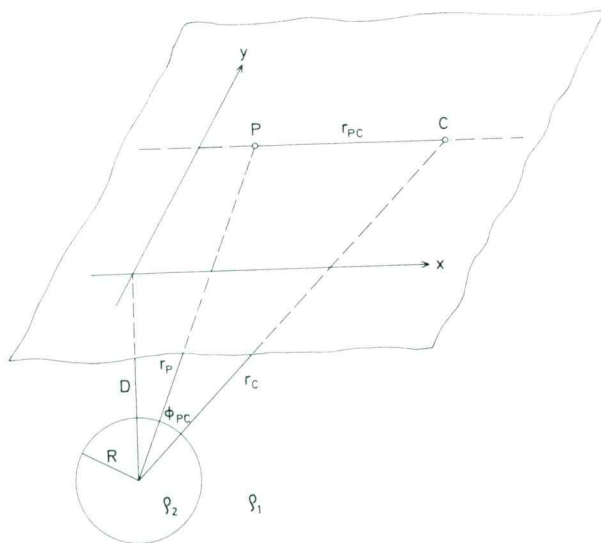


Fig. 10. Sphere in the homogeneous halfspace. ρ_2 and ρ_1 are the corresponding resistivities of the sphere and the halfspace, C is the point source (current electrode) and P the observation point (potential electrode)

Sl. 10. Krogla v homogenem polprostoru. ρ_2 in ρ_1 sta specifični električni upornosti krogle in polprostora, C je točkasti izvor toka (tokovna elektroda), P pa merska točka (merska ali potencialna elektroda)

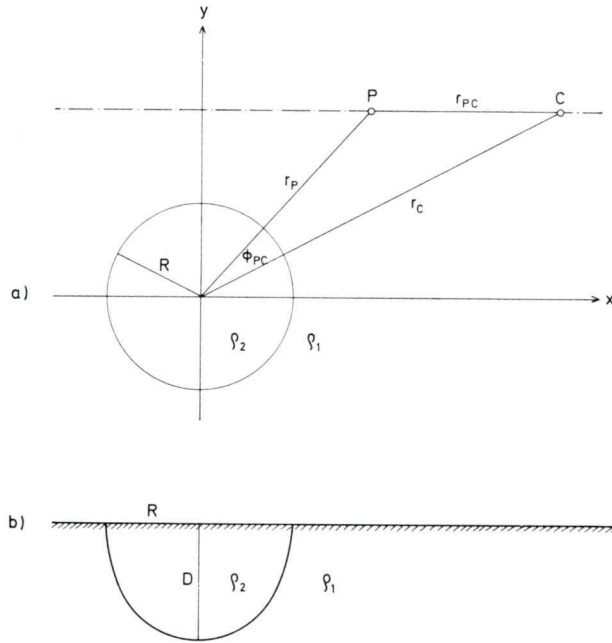


Fig. 11. Hemispheroid in homogeneous halfspace. a) Ground-plan and b) cross section

Sl. 11. Polsferoid v homogenem polprostoru. a) Tloris in b) vertikalni prerez skozi središče polsferoida

$$V = \frac{I\rho_1}{2\pi} \left[\frac{1}{r_{PC}} - \frac{2(\rho_1 - \rho_2)R}{r_P r_C} \sum_{n=1}^{\infty} \frac{n}{n(\rho_1 + \rho_2) + \rho_2} \left(\frac{R^2}{r_P r_C} \right)^n P_n(\cos \phi_{PC}) \right] \quad (1-1)$$

$$r_{PC} = |x_P - x_C| \quad r_P = \sqrt{x_P^2 + y^2 + D^2} \quad r_C = \sqrt{x_C^2 + y^2 + D^2} \quad \cos \phi_{PC} = \frac{r_P^2 + r_C^2 - r_{PC}^2}{2r_P r_C} \quad (1-a)$$

$$V_{11} = \frac{I\rho_1}{2\pi} \left[\frac{1}{r_{PC}} - \frac{(\rho_1 - \rho_2)R}{r_P r_C} \sum_{n=1}^{\infty} \frac{n}{n(\rho_1 + \rho_2) + \rho_2} \left(\frac{R^2}{r_P r_C} \right)^n P_n(\cos \phi_{PC}) \right] \quad (2-1)$$

$$V_{21} = \frac{I\rho_1}{2\pi} \left[\frac{1}{r_C} + \frac{\rho_2}{r_C} \sum_{n=1}^{\infty} \frac{2n + 1}{n(\rho_1 + \rho_2) + \rho_2} \left(\frac{r_P}{r_C} \right)^n P_n(\cos \phi_{PC}) \right] \quad (2-2)$$

$$V_{12} = \frac{I\rho_1}{2\pi} \left[\frac{1}{r_P} + \frac{\rho_2}{r_P} \sum_{n=1}^{\infty} \frac{2n + 1}{n(\rho_1 + \rho_2) + \rho_2} \left(\frac{r_C}{r_P} \right)^n P_n(\cos \phi_{PC}) \right] \quad (2-3)$$

$$V_{22} = \frac{I\rho_1}{2\pi} \left[\frac{1}{R} + \rho_2 \left(\frac{1}{r_{PC}} - \frac{1}{R} \right) + \frac{\rho_2(\rho_1 - \rho_2)}{\rho_1 R} \sum_{n=1}^{\infty} \frac{n + 1}{n(\rho_1 + \rho_2) + \rho_2} \left(\frac{r_C r_P}{R^2} \right)^n P_n(\cos \phi_{PC}) \right] \quad (2-4)$$

$$r_{PC} = |x_P - x_C| \quad r_P = \sqrt{x_P^2 + y^2} \quad r_C = \sqrt{x_C^2 + y^2} \quad \cos \phi_{PC} = \frac{r_P^2 + r_C^2 - r_{PC}^2}{2r_P r_C} \quad (2-a)$$

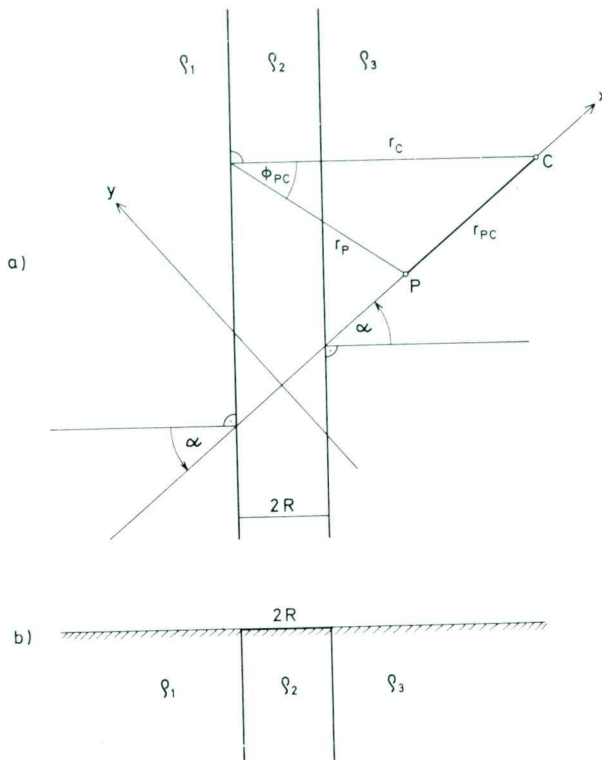


Fig. 12. Vertical dike in halfspace, consisting of two different homogeneous halves. a) Ground-plan and b) cross section

Sl. 12. Vertikalna plošča v polprostoru z dvema različnima homogenima polovicama. a) Tloris, b) prečni prerez

Nostrand (1954). They have been slightly transformed in order to be more suitable for numerical processing.

As the model of a deep-seated bauxite deposit usually horizontally elongated, a vertical dike of unlimited length and depth seems to be appropriate. The solution of Laplace's differential equation for vertical dikes is given by V. K. Hmelevskoj (1970) specifically for the case where the survey line traverses the dike at right angles. The equations (3-1) to (3-9) have been deduced for an arbitrary direction of the strike of the dike. The meaning of the symbols is evident in fig. 12 and equation (3-a). As shown in the figure, the dike halves the space into those parts designated "1" and "3". Both structures ought not to differ considerably one from the other in the present case, since they consist of Eocene and possibly of Cretaceous limestone. Owing to their different moisture contents and low-resistivity material, the resistivities pertaining to each side of the bauxite deposit might be different. Assuming that the shape of all the remaining models varies between the hemispheroid and dike, the corresponding influence may be assessed by interpolation.

$$V_{11} = \frac{I_{D1}}{2\pi} \left[\frac{1}{r_{PC}} - \frac{k_{21}}{\sqrt{r_p^2 + r_C^2 + 2r_p r_C \cos \phi_{PC}}} + k_{23} (1 - k_{21}^2) \sum_{n=0}^{\infty} \frac{(k_{21} k_{23})^n}{\sqrt{r_p^2 + [4(n+1)R + r_C]^2 + 2r_p [4(n+1)R + r_C] \cos \phi_{PC}}} \right] \quad (3-1)$$

$$V_{21} = \frac{I_{D2}(1+k_{21})}{2\pi} \sum_{n=0}^{\infty} (k_{21} k_{23})^n \left[\frac{1}{\sqrt{r_p^2 + [4nR + r_C]^2 - 2r_p [4nR + r_C] \cos \phi_{PC}}} + \frac{k_{23}}{\sqrt{r_p^2 + [4(n+1)R + r_C]^2 + 2r_p [4(n+1)R + r_C] \cos \phi_{PC}}} \right] \quad (3-2)$$

$$V_{31} = \frac{I_{D3}(1+k_{21})(1-k_{23})}{2\pi} \sum_{n=0}^{\infty} \frac{(k_{21} k_{23})^n}{\sqrt{r_p^2 + [4nR + r_C]^2 - 2r_p [4nR + r_C] \cos \phi_{PC}}} \quad (3-3)$$

$$V_{12} = \frac{I_{D1}(1-k_{21})}{2\pi} \sum_{n=0}^{\infty} (k_{21} k_{23})^n \left[\frac{1}{\sqrt{r_p^2 + [4nR + r_C]^2 - 2r_p [4nR + r_C] \cos \phi_{PC}}} + \frac{k_{23}}{\sqrt{r_p^2 + [4(n+1)R - r_C]^2 - 2r_p [4(n+1)R - r_C] \cos \phi_{PC}}} \right] \quad (3-4)$$

$$V_{22} = \frac{I_{D2}}{2\pi} \left\{ \frac{1}{r_{PC}} + \sum_{n=0}^{\infty} (k_{21} k_{23})^n \left[\frac{k_{21}}{\sqrt{r_p^2 + [4nR + r_C]^2 + 2r_p [4nR + r_C] \cos \phi_{PC}}} + \frac{k_{23}}{\sqrt{r_p^2 + [4(n+1)R - r_C]^2 - 2r_p [4(n+1)R - r_C] \cos \phi_{PC}}} + \frac{k_{21} k_{23}}{\sqrt{r_p^2 + [4(n+1)R + r_C]^2 - 2r_p [4(n+1)R + r_C] \cos \phi_{PC}}} + \frac{k_{21} k_{23}}{\sqrt{r_p^2 + [4(n+1)R - r_C]^2 + 2r_p [4(n+1)R - r_C] \cos \phi_{PC}}} \right] \right\} \quad (3-5)$$

$$V_{32} = \frac{I_{D3}(1-k_{21})}{2\pi} \sum_{n=0}^{\infty} (k_{21} k_{23})^n \left[\frac{1}{\sqrt{r_p^2 + [4nR - r_C]^2 + 2r_p [4nR - r_C] \cos \phi_{PC}}} + \frac{k_{21} k_{23}}{\sqrt{r_p^2 + [4nR + r_C]^2 + 2r_p [4nR + r_C] \cos \phi_{PC}}} \right] \quad (3-6)$$

$$V_{13} = \frac{I_{D1}(1-k_{21})(1+k_{23})}{2\pi} \sum_{n=0}^{\infty} \frac{(k_{21} k_{23})^n}{\sqrt{r_p^2 + [4nR + r_C]^2 - 2r_p [4nR + r_C] \cos \phi_{PC}}} \quad (3-7)$$

$$V_{23} = \frac{I_{D2}(1+k_{23})}{2\pi} \sum_{n=0}^{\infty} (k_{21} k_{23})^n \left[\frac{1}{\sqrt{r_p^2 + [4nR + r_C]^2 - 2r_p [4nR + r_C] \cos \phi_{PC}}} + \frac{k_{21}}{\sqrt{r_p^2 + [4nR + r_C]^2 + 2r_p [4nR + r_C] \cos \phi_{PC}}} \right] \quad (3-8)$$

$$V_{33} = \frac{I_{D3}}{2\pi} \left[\frac{1}{r_{PC}} - \frac{k_{23}}{\sqrt{r_p^2 + [4R - r_C]^2 - 2r_p [4R - r_C] \cos \phi_{PC}}} + k_{21} (1 - k_{23}^2) \sum_{n=0}^{\infty} \frac{(k_{21} k_{23})^n}{\sqrt{r_p^2 + [4nR + r_C]^2 + 2r_p [4nR + r_C] \cos \phi_{PC}}} \right] \quad (3-9)$$

$$r_{PC} = ||x_p^2 - |x_C||$$

$$r_C = ||x_C| \cos \alpha \pm R| \quad \left\{ \begin{array}{l} + R \dots x_C \geq 0 \\ - R \dots x_C < 0 \end{array} \right.$$

$$r_p = \sqrt{r_{PC}^2 + r_C^2 - 2r_{PC} r_C \cos \alpha}$$

$$\cos \phi_{PC} = \frac{r_p^2 + r_C^2 - r_{PC}^2}{2r_p r_C}$$

$$k_{ij} = \frac{\rho_j - \rho_i}{\rho_j + \rho_i}$$

(3-a)

$$V_{11} = \frac{I\rho_1}{2\pi} \left\{ \frac{1}{r_{PC}} - \frac{\rho_1 - \rho_2}{f} \sum_{n=1}^{\infty} \sum_{m=0}^n \frac{(2n+1)(2-\delta)}{(-1)^m} \frac{[(n-m)!]^2}{[(n+m)!]^2} \frac{K_n^m(\eta_R)L_n^m(\eta_R)}{\rho_1 L_n^m(\eta_R) - \rho_2 K_n^m(\eta_R)} [P_n^m(0)]^2 Q_n^m(\eta_P)Q_n^m(\eta_C) \cos m\phi_{PC} \right\} \quad (4-1)$$

$$V_{21} = \frac{I\rho_1}{2\pi} \left\{ \frac{1}{r_{PC}} - \frac{\rho_1 - \rho_2}{f} \sum_{n=1}^{\infty} \sum_{m=0}^n \frac{(2n+1)(2-\delta)}{(-1)^m} \frac{[(n-m)!]^2}{[(n+m)!]^2} \frac{L_n^m(\eta_R)}{\rho_1 L_n^m(\eta_R) - \rho_2 K_n^m(\eta_R)} [P_n^m(0)]^2 P_n^m(\eta_P)Q_n^m(\eta_C) \cos m\phi_{PC} \right\} \quad (4-2)$$

$$V_{12} = \frac{I\rho_1}{2\pi} \left\{ \frac{\rho_2}{\rho_1 r_{PC}} - \frac{\rho_2(\rho_1 - \rho_2)}{\rho_1 f} \sum_{n=1}^{\infty} \sum_{m=0}^n \frac{(2n+1)(2-\delta)}{(-1)^m} \frac{[(n-m)!]^2}{[(n+m)!]^2} \frac{K_n^m(R)}{\rho_1 L_n^m(\eta_R) - \rho_2 K_n^m(\eta_R)} [P_n^m(0)]^2 Q_n^m(\eta_P)P_n^m(\eta_C) \cos m\phi_{PC} + \frac{\rho_1 - \rho_2}{\rho_1 f} Q_0(\eta_P) \right\} \quad (4-3)$$

$$V_{22} = \frac{I\rho_1}{2\pi} \left\{ \frac{\rho_2}{\rho_1 r_{PC}} - \frac{\rho_2(\rho_1 - \rho_2)}{\rho_1 f} \sum_{n=1}^{\infty} \sum_{m=0}^n \frac{(2n+1)(2-\delta)}{(-1)^m} \frac{[(n-m)!]^2}{[(n+m)!]^2} \frac{1}{\rho_1 L_n^m(\eta_R) - \rho_2 K_n^m(\eta_R)} [P_n^m(0)]^2 P_n^m(\eta_P)P_n^m(\eta_C) \cos m\phi_{PC} + \frac{\rho_1 - \rho_2}{\rho_1 f} Q_0(\eta_R) \right\} \quad (4-4)$$

$$\left. \begin{aligned} f &= \sqrt{|D^2 - R^2|} \\ \delta &= \begin{cases} 1 & \dots \dots m=0 \\ 0 & \dots \dots m \neq 0 \end{cases} \\ K_n^m(\eta_R) &= \frac{P_n^m(\eta_R)}{Q_n^m(\eta_R)} & L_n^m(\eta_R) &= \frac{P_n^m(\eta_R)}{Q_n^m(\eta_R)} \\ \eta_R &= \sqrt{\left(\frac{R}{f}\right)^2 + 1} & \eta_P &= \sqrt{\left(\frac{r_P}{f}\right)^2 + 1} & \eta_C &= \sqrt{\left(\frac{r_C}{f}\right)^2 + 1} \\ r_{PC} &= |x_P - x_C| & r_P &= \sqrt{x_P^2 + y^2} & r_C &= \sqrt{x_C^2 + y^2} & \cos \phi_{PC} &= \frac{r_P^2 + r_C^2 - r_{PC}^2}{2r_P r_C} \end{aligned} \right\} \quad (4-a)$$

$$V_{11} = \frac{I\rho_1}{2\pi} \left\{ \frac{1}{r_{PC}} - \frac{\rho_1 - \rho_2}{f} \sum_{n=1}^{\infty} \sum_{m=0}^n \frac{i(2n+1)(2-\delta)}{(-1)^m} \frac{[(n-m)!]^2}{[(n+m)!]^2} \frac{K_n^m(i\zeta_R)L_n^m(i\zeta_R)}{\rho_1 L_n^m(i\zeta_R) - \rho_2 K_n^m(i\zeta_R)} [P_n^m(0)]^2 Q_n^m(i\zeta_P)Q_n^m(i\zeta_C) \cos m\phi_{PC} \right\} \quad (5-1)$$

$$V_{21} = \frac{I\rho_1}{2\pi} \left\{ \frac{1}{r_{PC}} - \frac{\rho_1 - \rho_2}{f} \sum_{n=1}^{\infty} \sum_{m=0}^n \frac{i(2n+1)(2-\delta)}{(-1)^m} \frac{[(n-m)!]^2}{[(n+m)!]^2} \frac{L_n^m(i\zeta_R)}{\rho_1 L_n^m(i\zeta_R) - \rho_2 K_n^m(i\zeta_R)} [P_n^m(0)]^2 P_n^m(i\zeta_P)Q_n^m(i\zeta_C) \cos m\phi_{PC} \right\} \quad (5-2)$$

$$V_{12} = \frac{I\rho_1}{2\pi} \left\{ \frac{\rho_2}{\rho_1 r_{PC}} - \frac{\rho_2(\rho_1 - \rho_2)}{\rho_1 f} \sum_{n=1}^{\infty} \sum_{m=0}^n \frac{i(2n+1)(2-\delta)}{(-1)^m} \frac{[(n-m)!]^2}{[(n+m)!]^2} \frac{K_n^m(i\zeta_R)}{\rho_1 L_n^m(i\zeta_R) - \rho_2 K_n^m(i\zeta_R)} [P_n^m(0)]^2 Q_n^m(i\zeta_P)P_n^m(i\zeta_C) \cos m\phi_{PC} + \frac{\rho_1 - \rho_2}{\rho_1 f} \arctan \left(\frac{1}{\zeta_P}\right) \right\} \quad (5-3)$$

$$V_{22} = \frac{I\rho_1}{2\pi} \left\{ \frac{\rho_2}{\rho_1 r_{PC}} - \frac{\rho_2(\rho_1 - \rho_2)}{\rho_1 f} \sum_{n=1}^{\infty} \sum_{m=0}^n \frac{i(2n+1)(2-\delta)}{(-1)^m} \frac{[(n-m)!]^2}{[(n+m)!]^2} \frac{1}{\rho_1 L_n^m(i\zeta_R) - \rho_2 K_n^m(i\zeta_R)} [P_n^m(0)]^2 P_n^m(i\zeta_P)P_n^m(i\zeta_C) \cos m\phi_{PC} + \frac{\rho_1 - \rho_2}{\rho_1 f} \arctan \left(\frac{1}{\zeta_R}\right) \right\} \quad (5-4)$$

$$\begin{aligned}
 K_n^m(i\zeta_R) &= \frac{P_n^m(i\zeta_R)}{Q_n^m(i\zeta_R)} & L_n^m(i\zeta_R) &= \frac{P_n^{*m}(i\zeta_R)}{Q_n^{*m}(i\zeta_R)} \\
 \delta &= \begin{cases} 1 & \dots m = 0 \\ 0 & \dots m \neq 0 \end{cases} & f &= \sqrt{D^2 - R^2} & \zeta_R &= \sqrt{\left(\frac{R}{f}\right)^2 - 1} \\
 \zeta_P &= \sqrt{\left(\frac{r_P}{f}\right)^2 - 1} = \begin{cases} \sqrt{\left(\frac{r_P}{f}\right)^2 - 1} & \dots P_n^m(i\zeta_P) + P_n^m(i\zeta_P) \\ i\sqrt{\left(\frac{r_P}{f}\right)^2 - 1} & \dots P_n^m(i\zeta_P) + i^{n+m} P_n^m(-i\zeta_P) \end{cases} & (5-a) \\
 \zeta_C &= \sqrt{\left(\frac{r_C}{f}\right)^2 - 1} = \begin{cases} \sqrt{\left(\frac{r_C}{f}\right)^2 - 1} & \dots P_n^m(i\zeta_C) + P_n^m(i\zeta_C) \\ i\sqrt{\left(\frac{r_C}{f}\right)^2 - 1} & \dots P_n^m(i\zeta_C) + i^{n+m} P_n^m(-i\zeta_C) \end{cases} \\
 R_{CP} &= |x_P - x_C| & r_P &= \sqrt{x_P^2 - y^2} & r_C &= \sqrt{x_C^2 + y^2} & \cos \Phi_{PC} &= \frac{r_P^2 + r_C^2 - r_{PC}^2}{2r_P r_C}
 \end{aligned}$$

2.2. Resistivity type curves

For qualitative as well as for quantitative interpretation, there are rather useful theoretical resistivity curves of various models available. Theoretical anomalies have been treated by several authors (K. L. C o o k and R. L. G r a y, 1961; K. L. C o o k and R. G. V a n N o s t r a n d, 1954). Some years ago a good selection of resistivity type curves for vertical dikes was published (K u m a r R a k e s h, 1973 — survey line perpendicular to the strike of the dike and electrodes along this line; S h. C. J a i n, 1974 — survey line perpendicular to the dike and electrode array perpendicular to this line). The published master curves were extremely useful in qualitative interpretation. However, in the first phase of quantitative evaluation, as well as for analysis and the examination of the characteristics of resistivity profiling, a more suitable collection of resistivity model curves was required.

All calculations were carried out by the Hewlet Packard 9830 A desk calculator. The hemisphere and the vertical dike served as basic models. In one particular case only the prolate and oblate spheroids were treated in order to reduce the duration of mathematical operations and problems of convergence. The calculated model curves are given in figs. 13 to 50. Most of the diagrams relate to the hemisphere (the deposits exhibiting a roughly circular subsidence for the most part) and to the Wenner electrode array. A survey of theoretical curves is given in table 1.

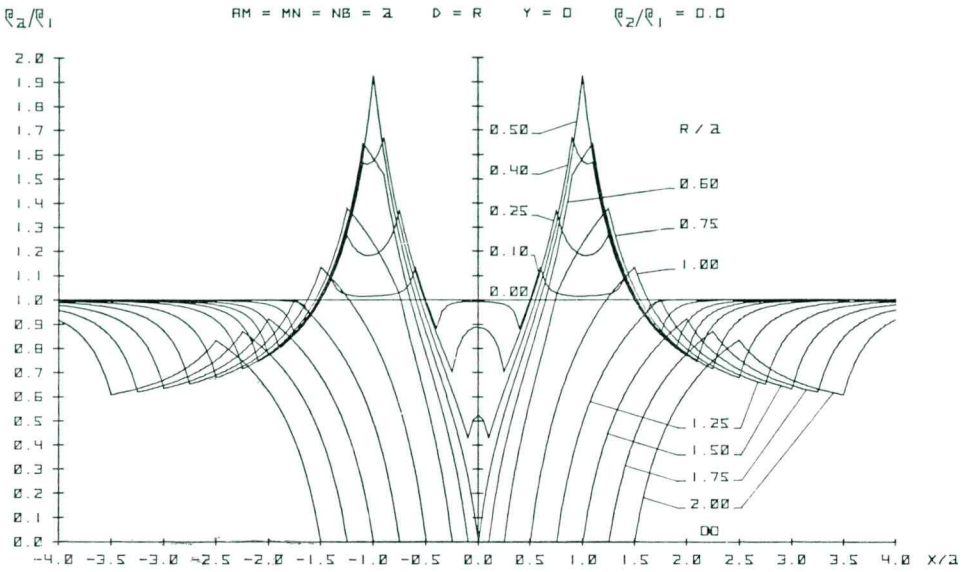


Fig. 13. Resistivity type curves over hemisphere
Sl. 13. Modelne krivulje polkrogle

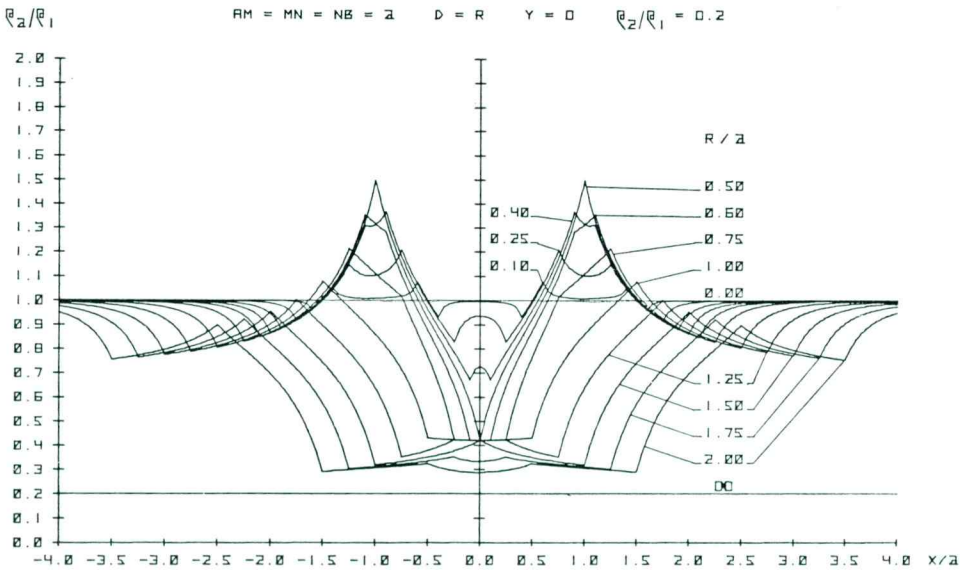


Fig. 14. Resistivity type curves over hemisphere
Sl. 14. Modelne krivulje polkrogle

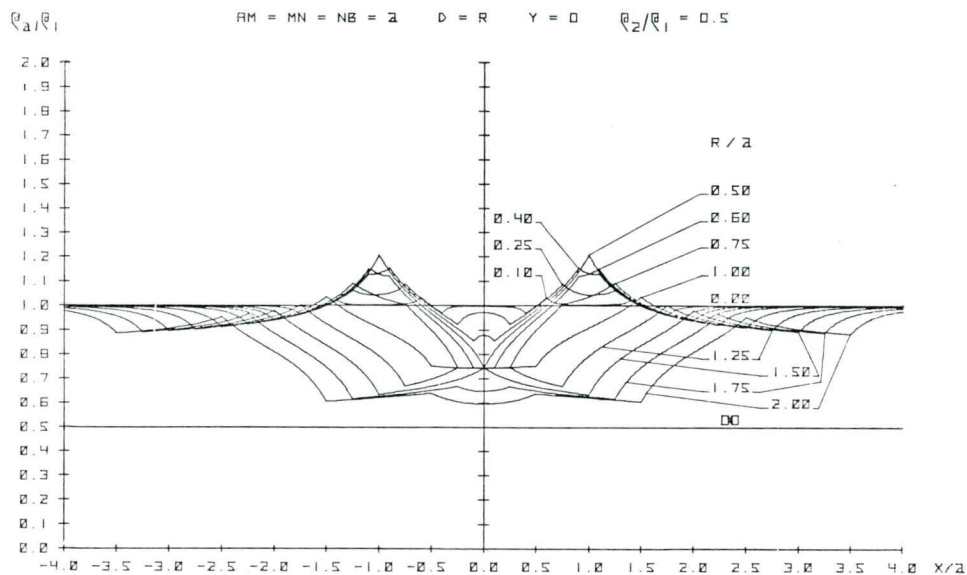


Fig. 15. Resistivity type curves over hemisphere
 Sl. 15. Modelne krivulje polkrogle

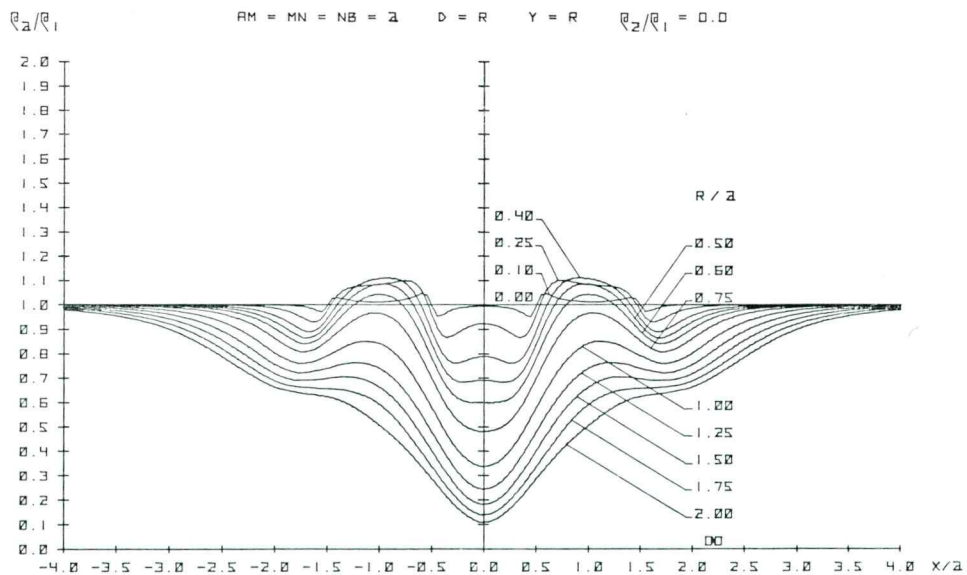


Fig. 16. Resistivity type curves over hemisphere
 Sl. 16. Modelne krivulje polkrogle

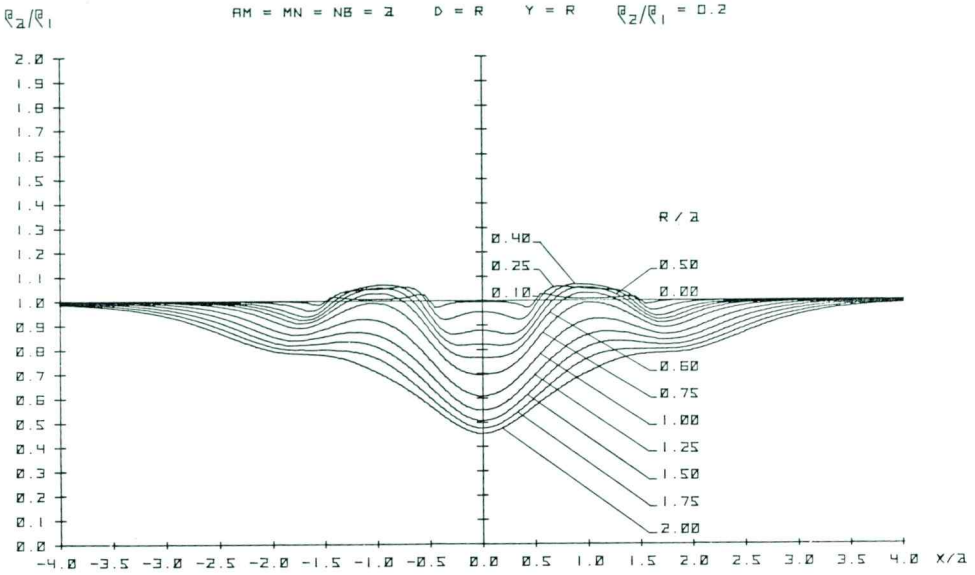


Fig. 17. Resistivity type curves over hemisphere
Sl. 17. Modelne krivulje polkrogle

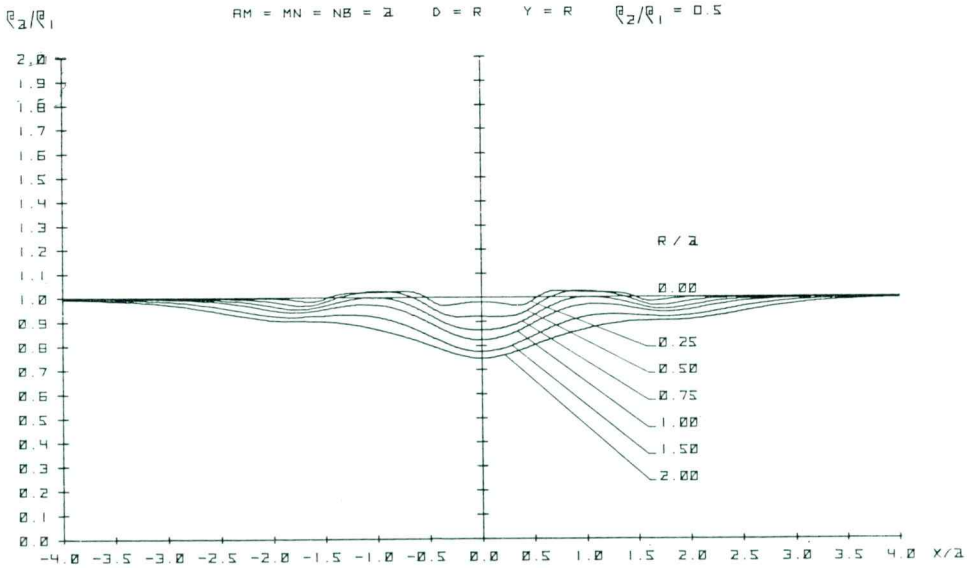


Fig. 18. Resistivity type curves over hemisphere
Sl. 18. Modelne krivulje polkrogle

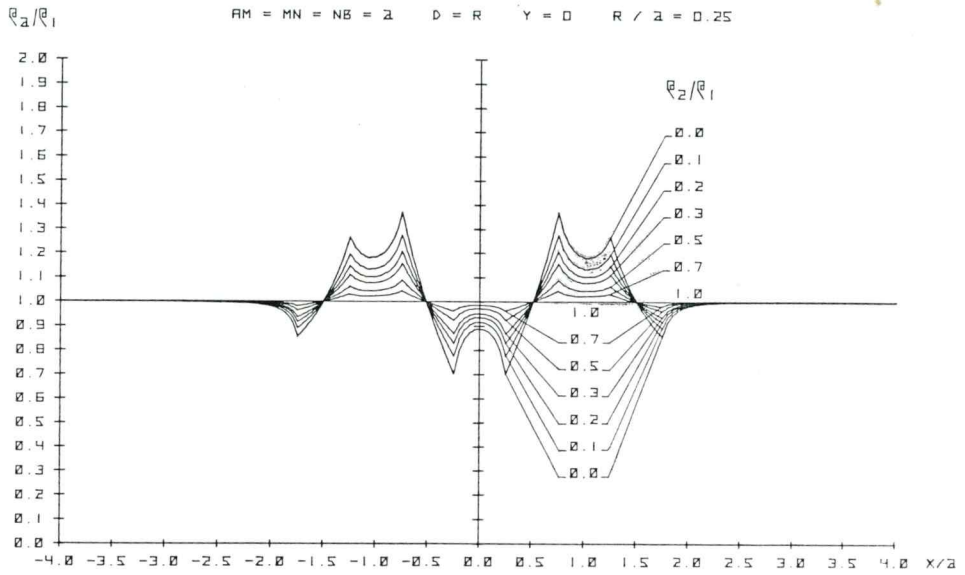


Fig. 19. Resistivity type curves over hemisphere
Sl. 19. Modelne krivulje polkrogle

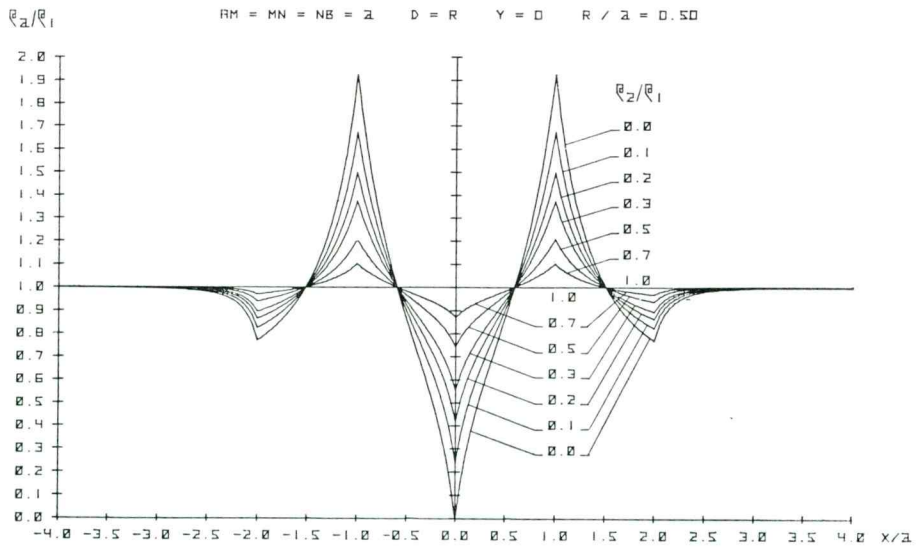


Fig. 20. Resistivity type curves over hemisphere
Sl. 20. Modelne krivulje polkrogle

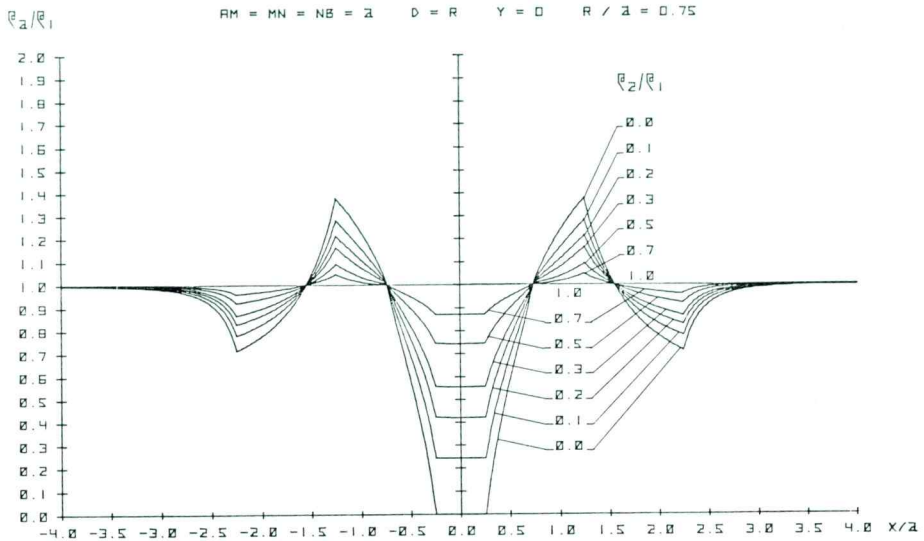


Fig. 21. Resistivity type curves over hemisphere
Sl. 21. Modelne krivulje polkrogle

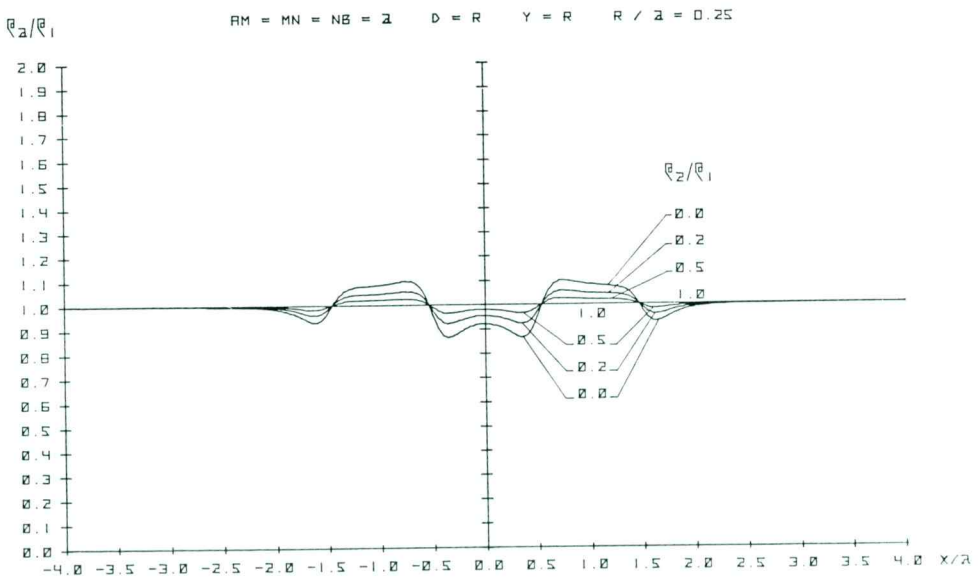


Fig. 22. Resistivity type curves over hemisphere
Sl. 22. Modelne krivulje polkrogle

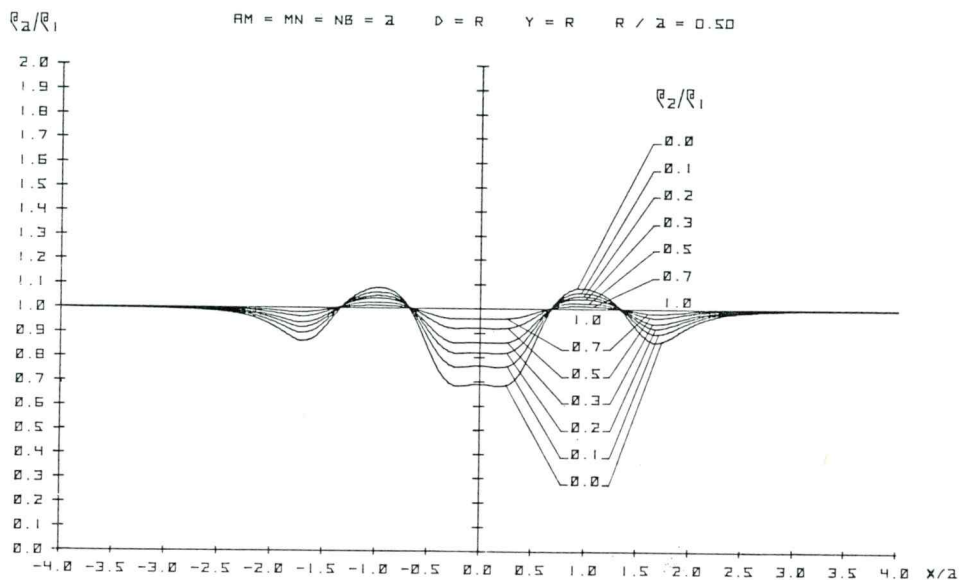


Fig. 23. Resistivity type curves over hemisphere
Sl. 23. Modelne krivulje polkrogle

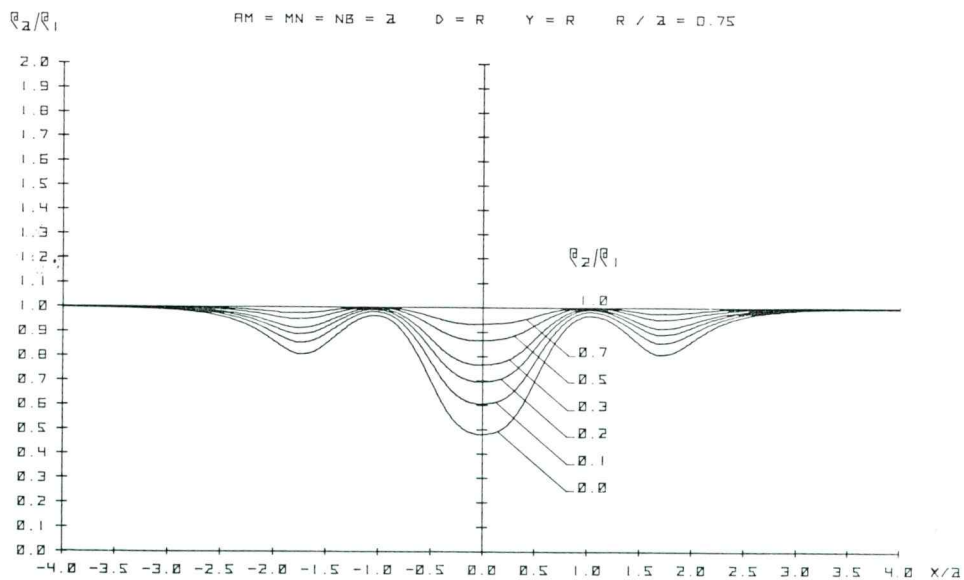


Fig. 24. Resistivity type curves over hemisphere
Sl. 24. Modelne krivulje polkrogle

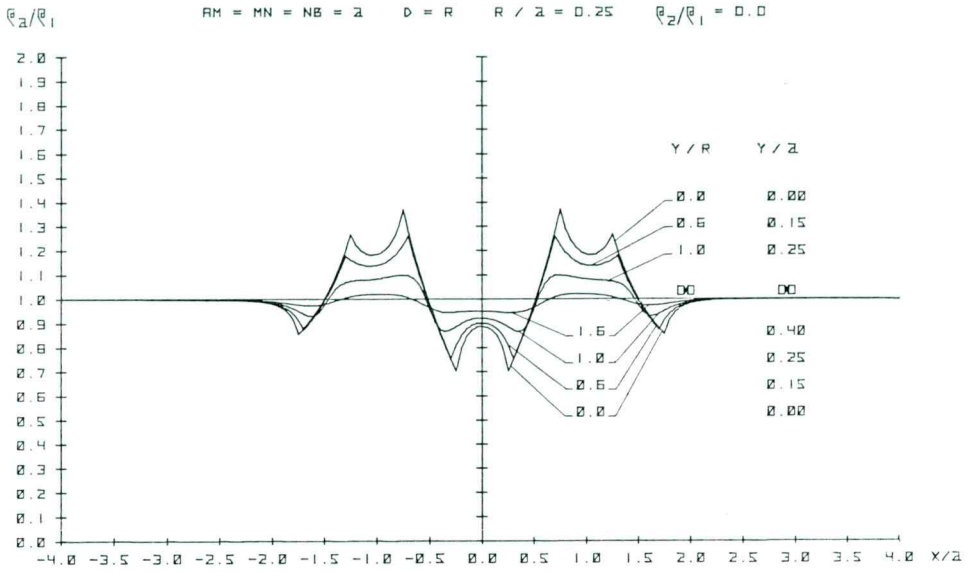


Fig. 25. Resistivity type curves over hemisphere
Sl. 25. Modelne krivulje polkrogle

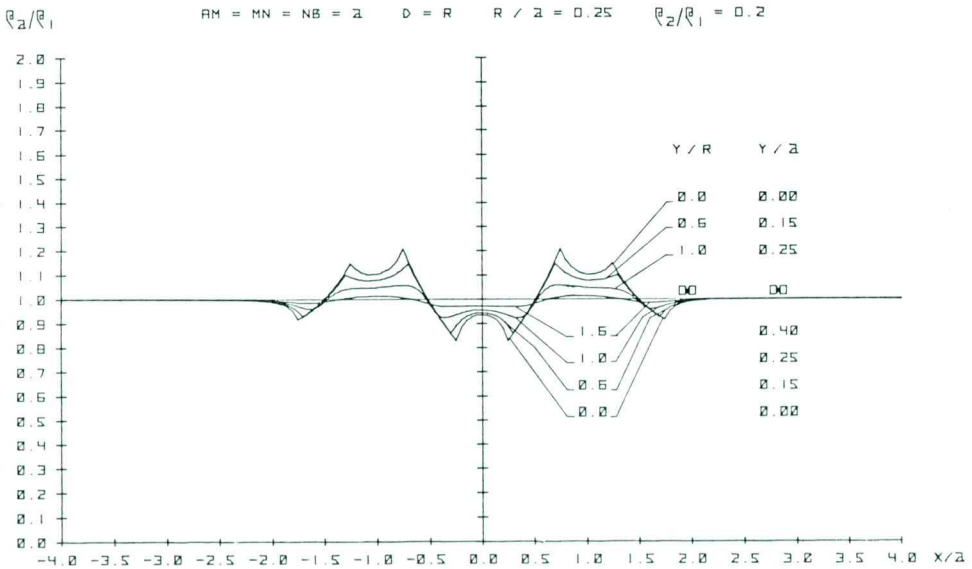


Fig. 26. Resistivity type curves over hemisphere
Sl. 26. Modelne krivulje polkrogle

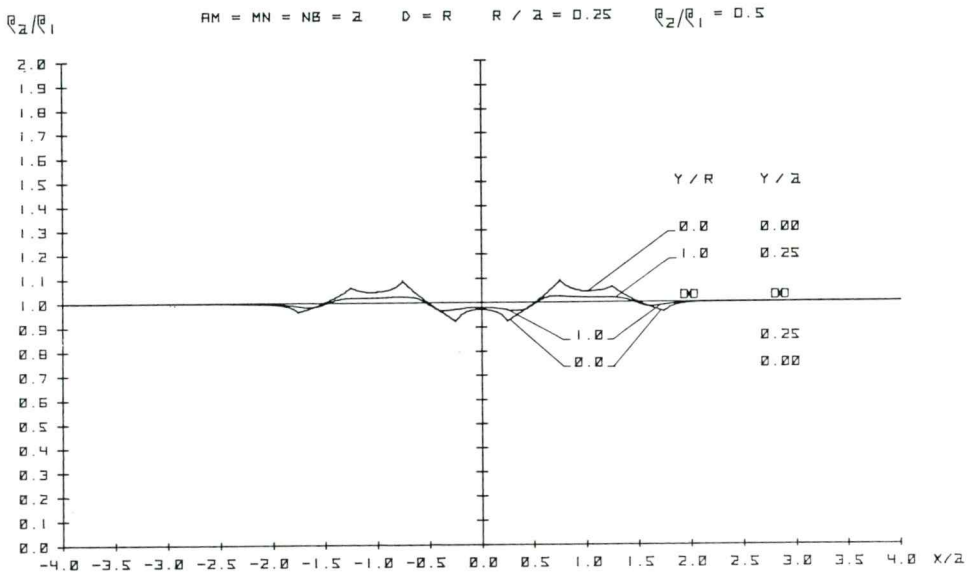


Fig. 27. Resistivity type curves over hemisphere
Sl. 27. Modelne krivulje polkrogle

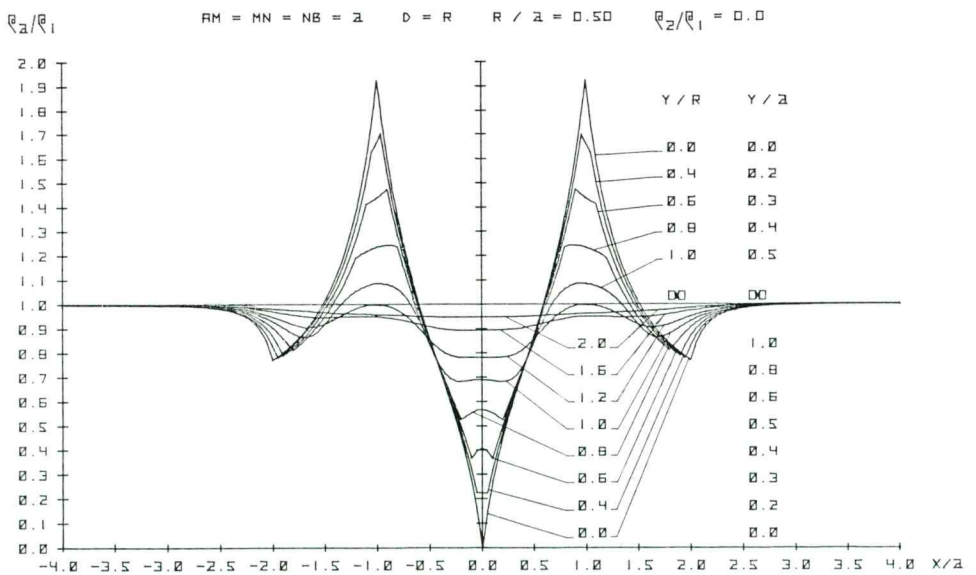


Fig. 28. Resistivity type curves over hemisphere
Sl. 28. Modelne krivulje polkrogle

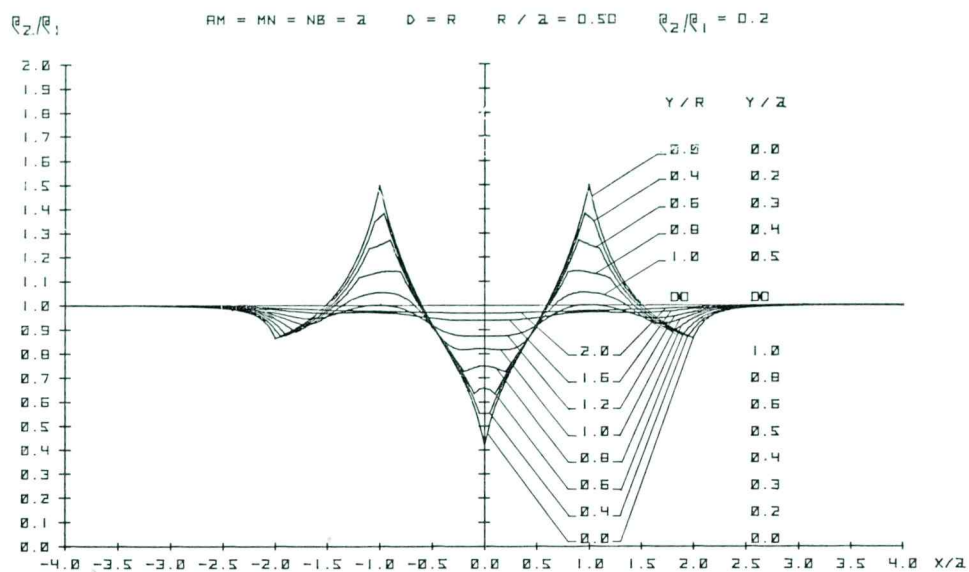


Fig. 29. Resistivity type curves over hemisphere
Sl. 29. Modelne krivulje polkrogle

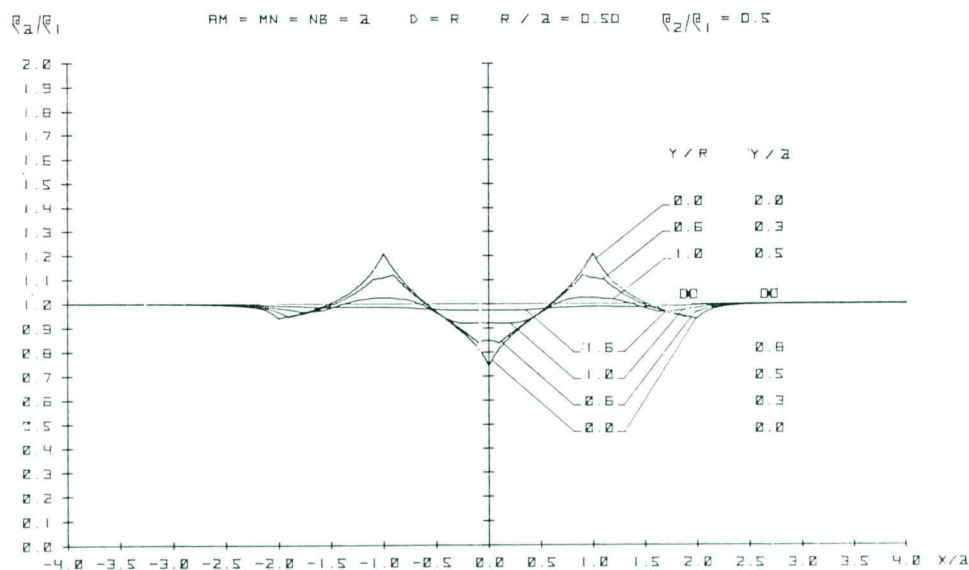


Fig. 30. Resistivity type curves over hemisphere
Sl. 30. Modelne krivulje polkrogle

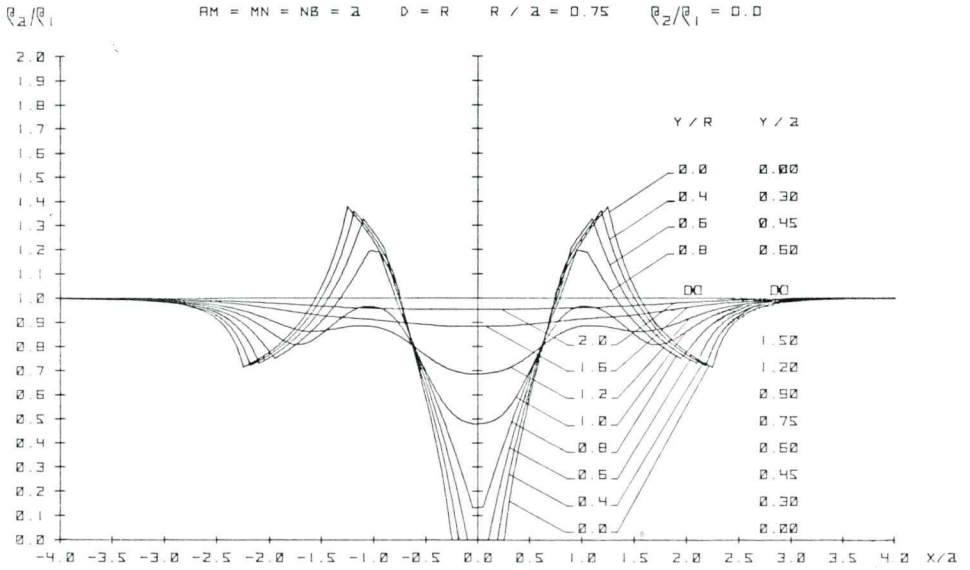


Fig. 31. Resistivity type curves over hemisphere
Sl. 31. Modelne krivulje polkrogle

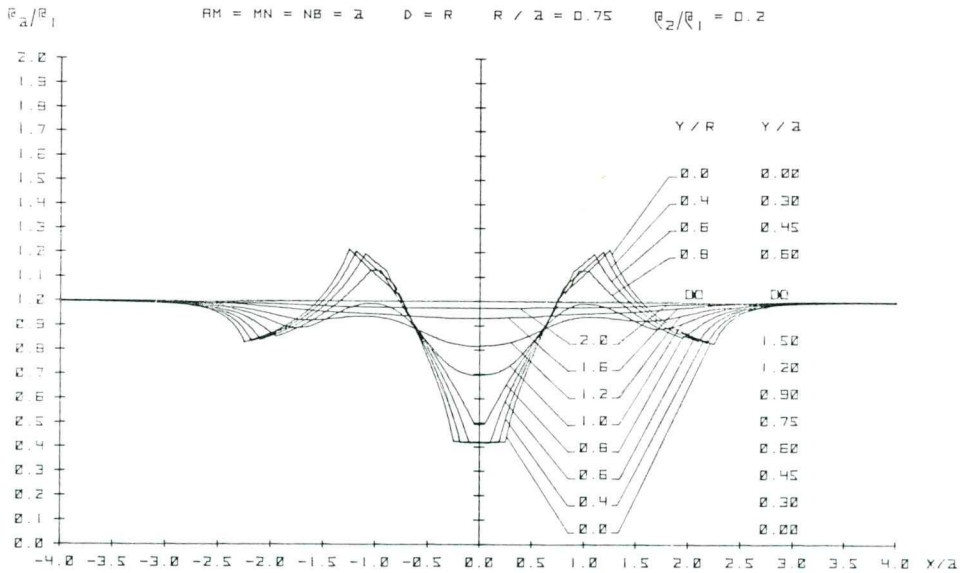


Fig. 32. Resistivity type curves over hemisphere
Sl. 32. Modelne krivulje polkrogle

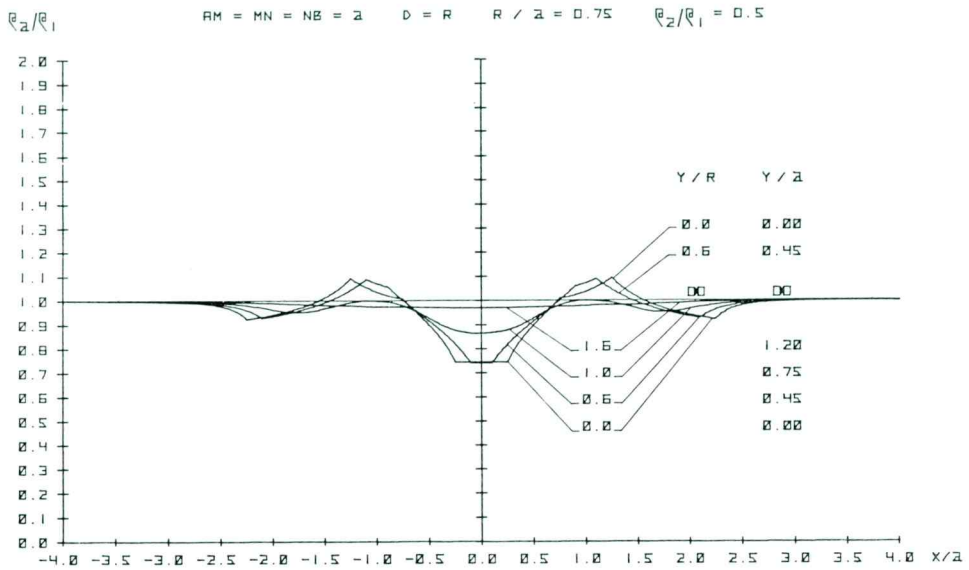


Fig. 33. Resistivity type curves over hemisphere
Sl. 33. Modelne krivulje polkrogle

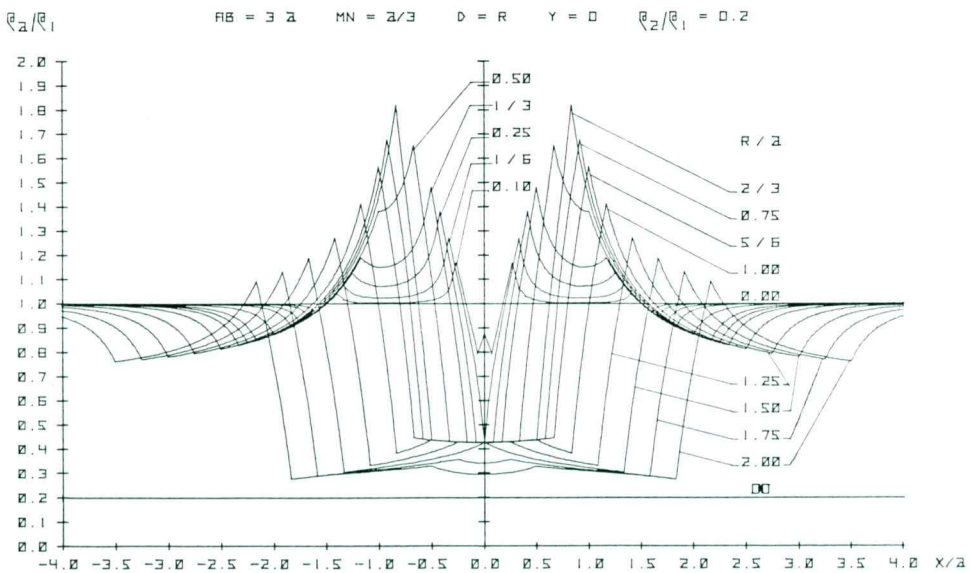


Fig. 34. Resistivity type curves over hemisphere
Sl. 34. Modelne krivulje polkrogle

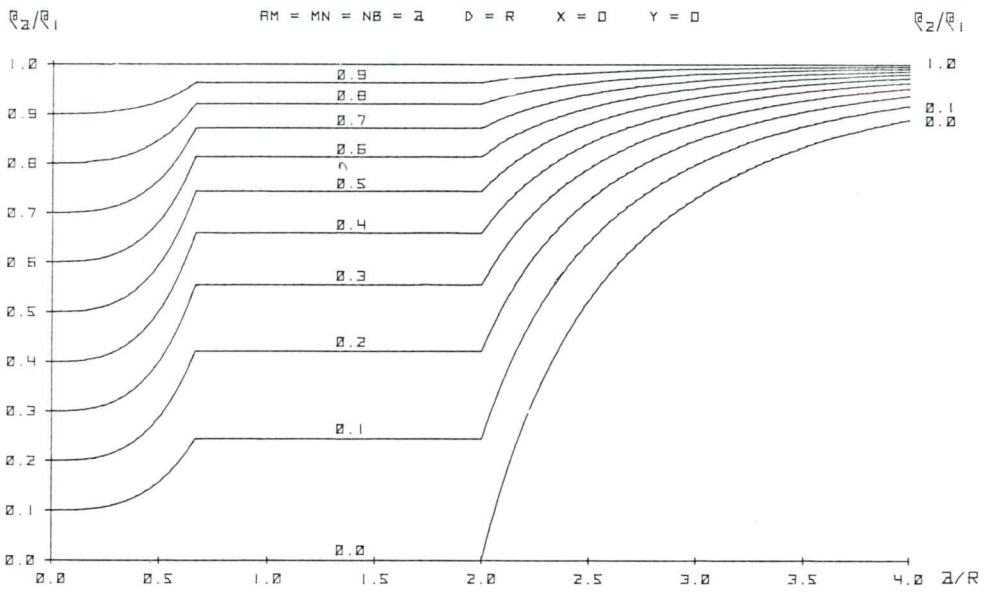


Fig. 35. Resistivity type curves over hemisphere
 Sl. 35. Modelne krivulje polkrogle

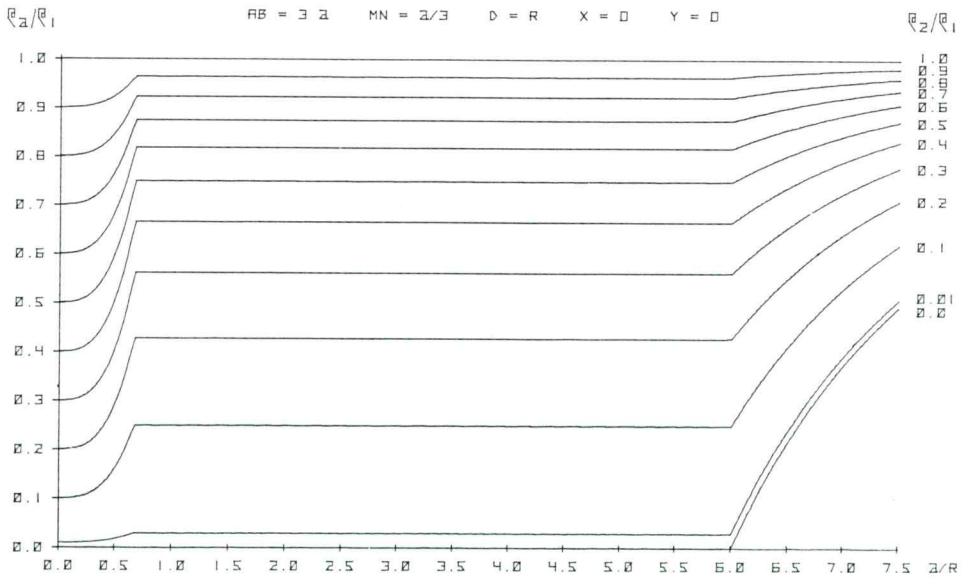


Fig. 36. Resistivity type curves over hemisphere
 Sl. 36. Modelne krivulje polkrogle

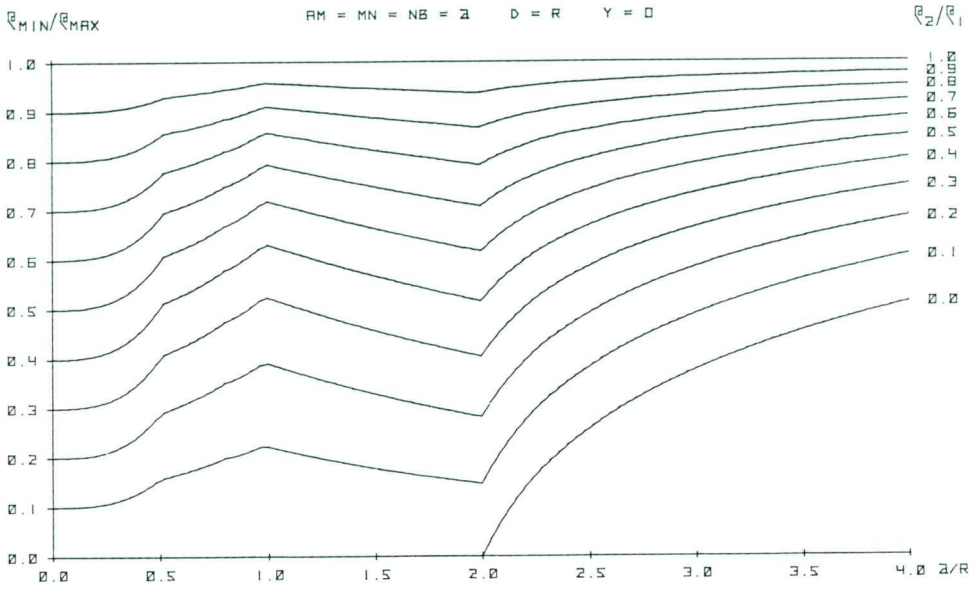


Fig. 37. Resistivity type curves over hemisphere
Sl. 37. Modelne krivulje polkrogle

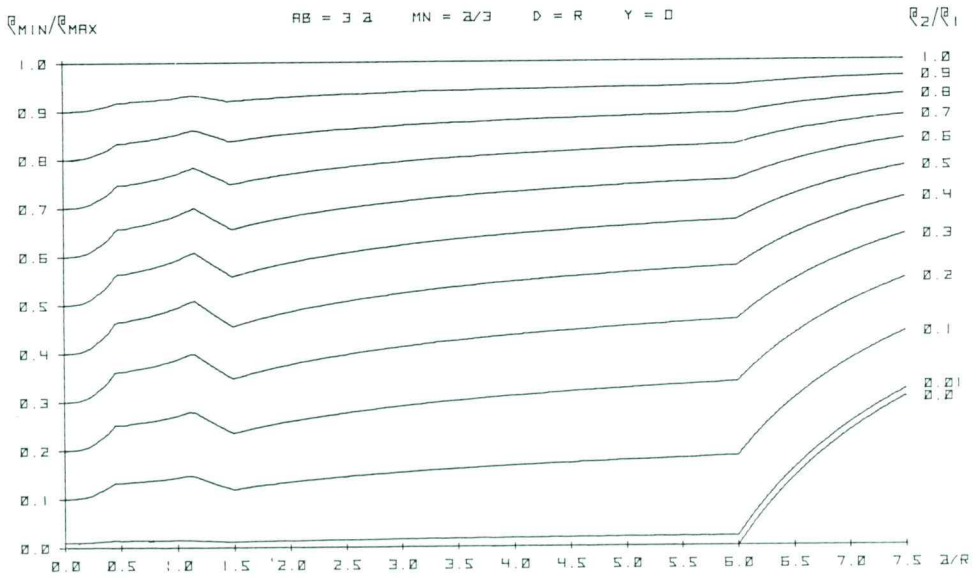


Fig. 38. Resistivity type curves over hemisphere
Sl. 38. Modelne krivulje polkrogle

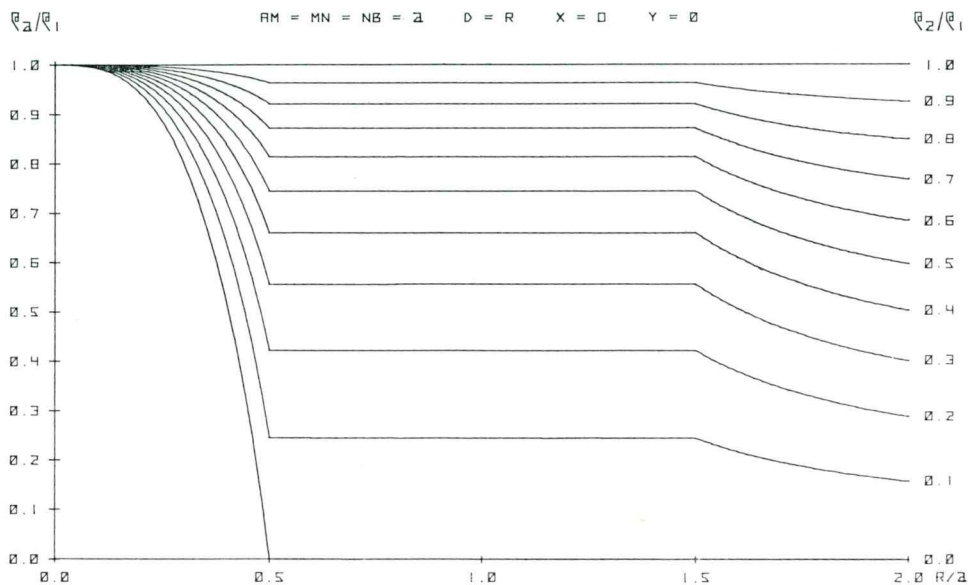


Fig. 39. Resistivity type curves over hemisphere
Sl. 39. Modelne krivulje polkrogle

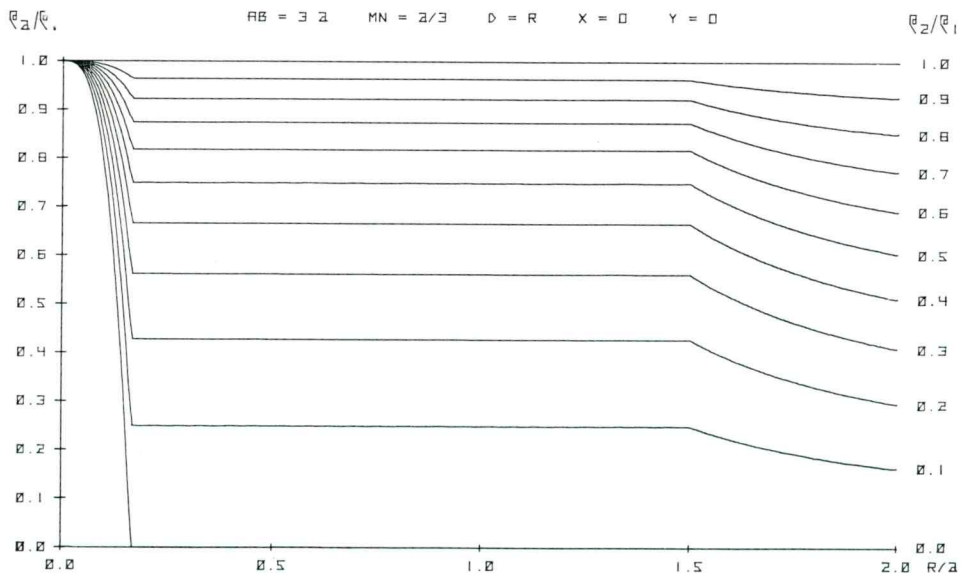


Fig. 40. Resistivity type curves over hemisphere
Sl. 40. Modelne krivulje polkrogle

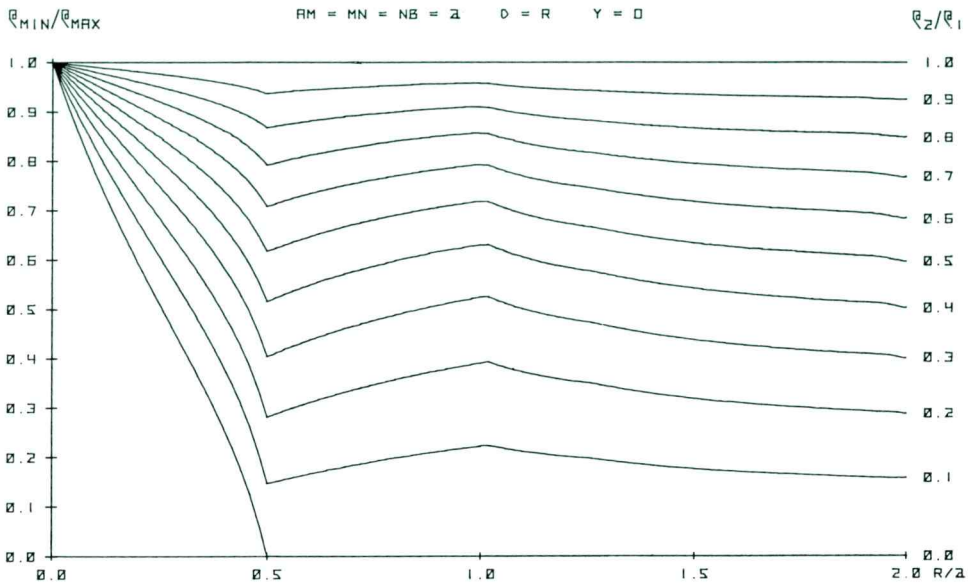


Fig. 41. Resistivity type curves over hemisphere
Sl. 41. Modelne krivulje polkrogle

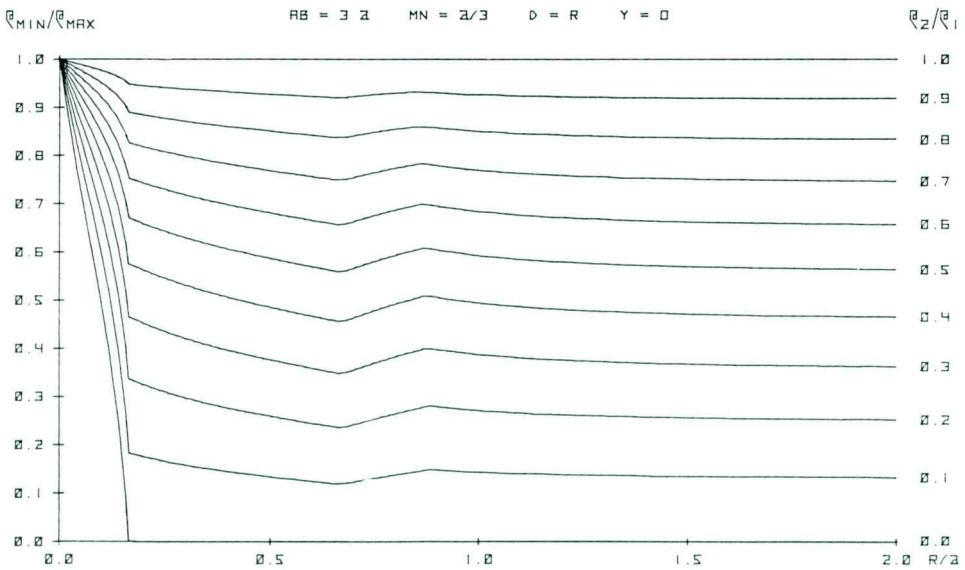


Fig. 42. Resistivity type curves over hemisphere
Sl. 42. Modelne krivulje polkrogle

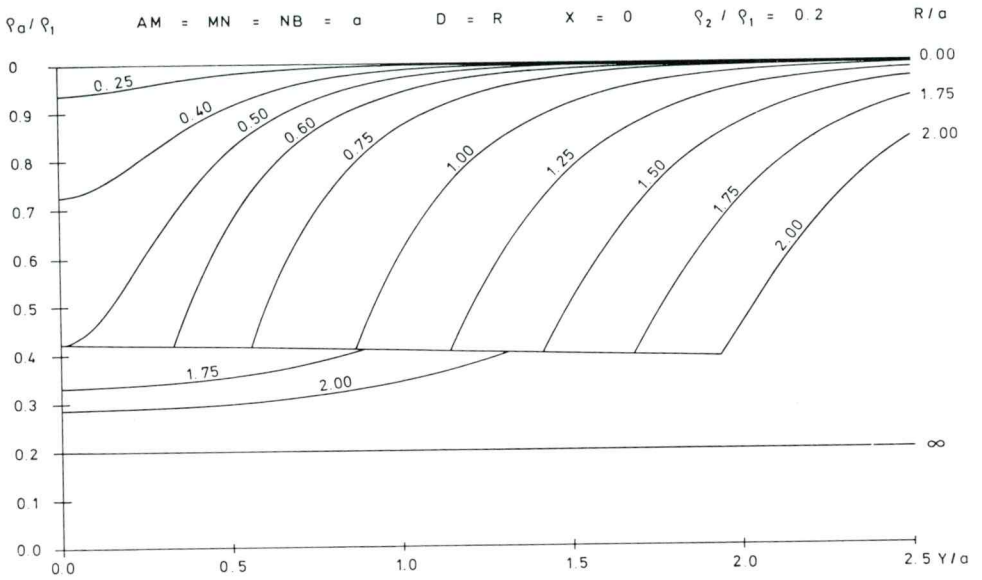


Fig. 43. Resistivity type curves over hemisphere
Sl. 43. Modelne krivulje polkrogle

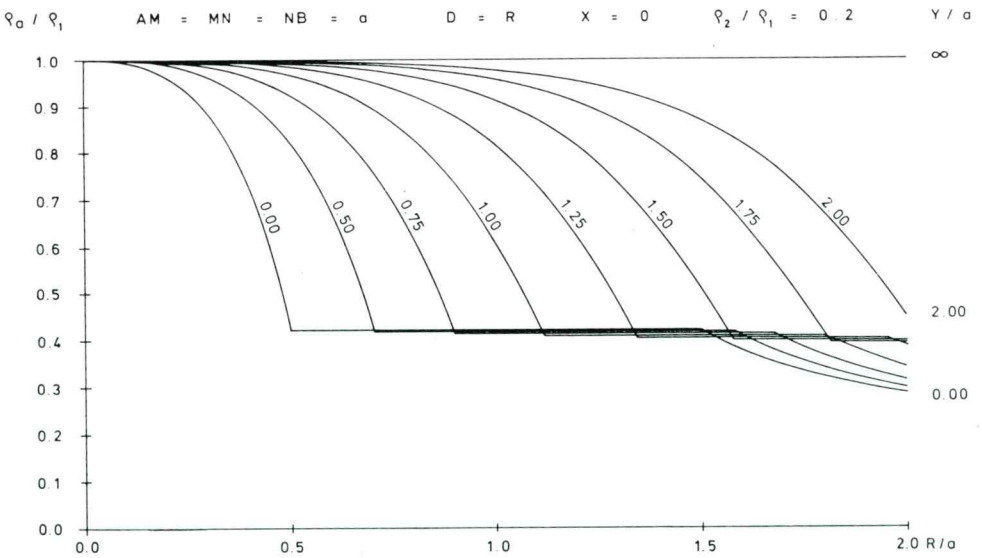
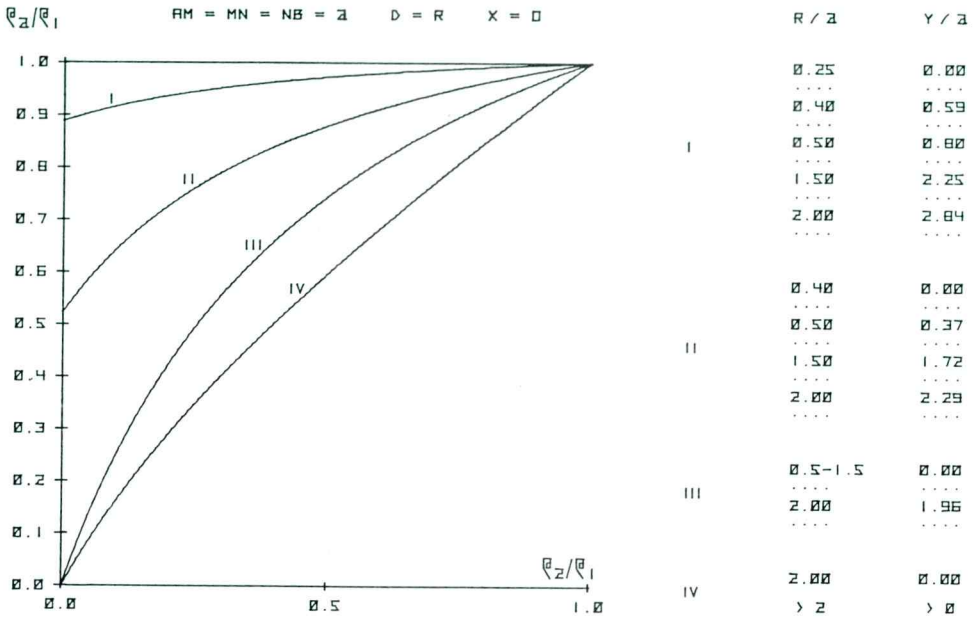


Fig. 44. Resistivity type curves over hemisphere
Sl. 44. Modelne krivulje polkrogle



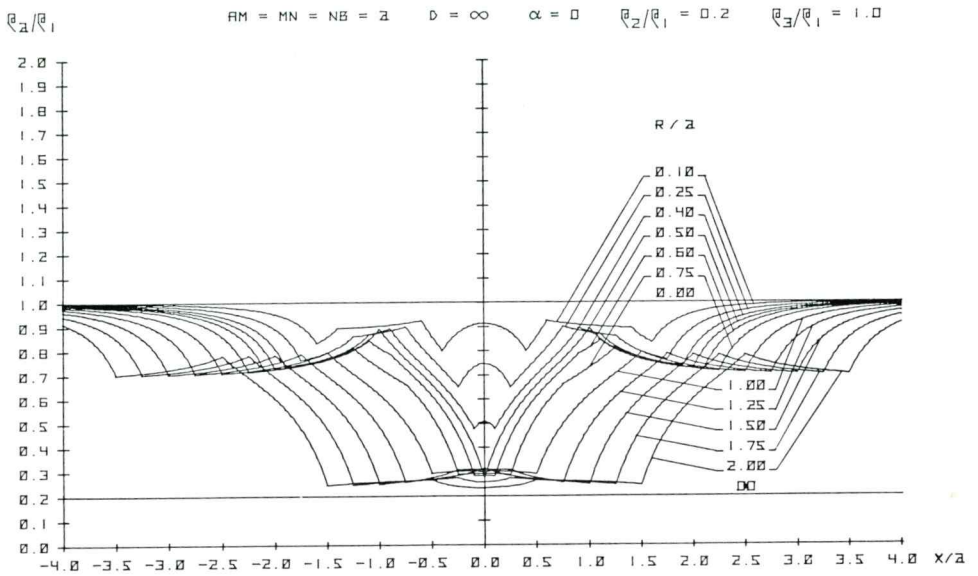


Fig. 46. Resistivity type curves over vertical dike
Sl. 46. Modelne krivulje vertikalne plošče

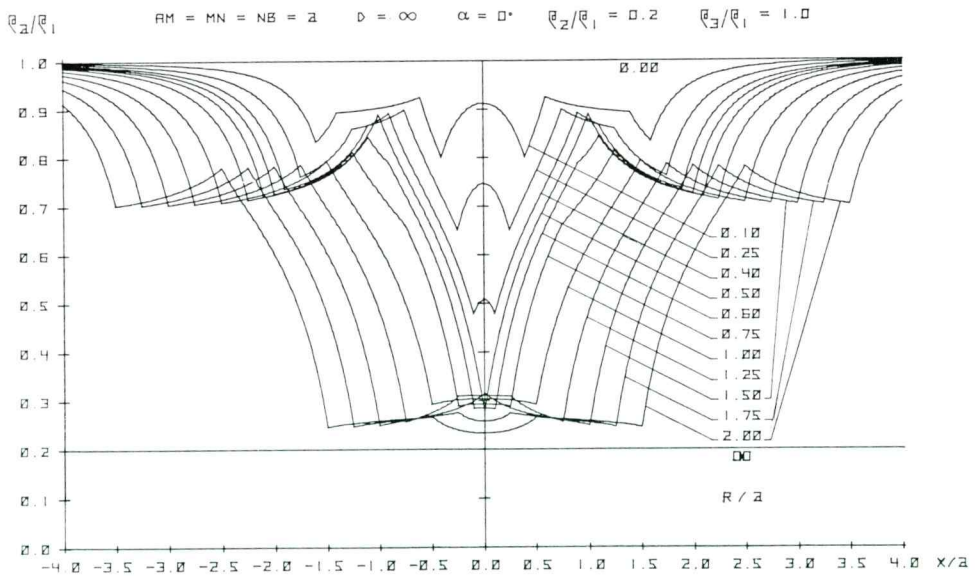


Fig. 46 a. Resistivity type curves over vertical dike
Sl. 46 a. Modelne krivulje vertikalne plošče

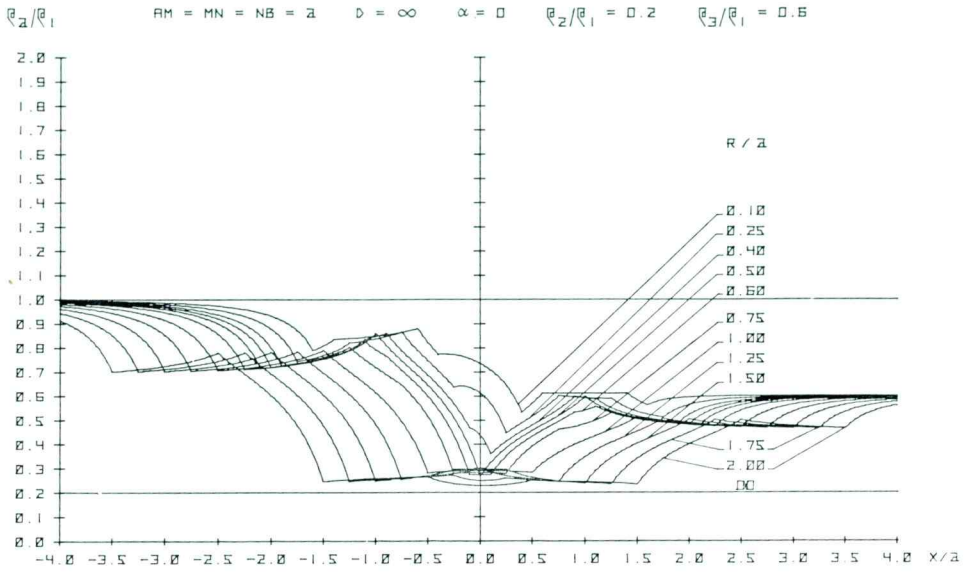


Fig. 47. Resistivity type curves over vertical dike
Sl. 47. Modelne krivulje vertikalne plošče

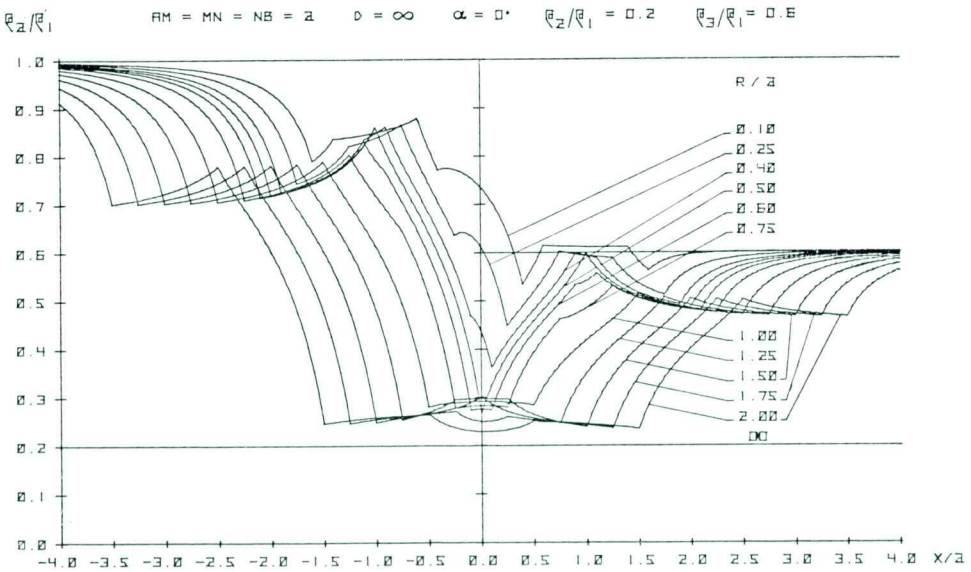


Fig. 47 a. Resistivity type curves over vertical dike
Sl. 47 a. Modelne krivulje vertikalne plošče

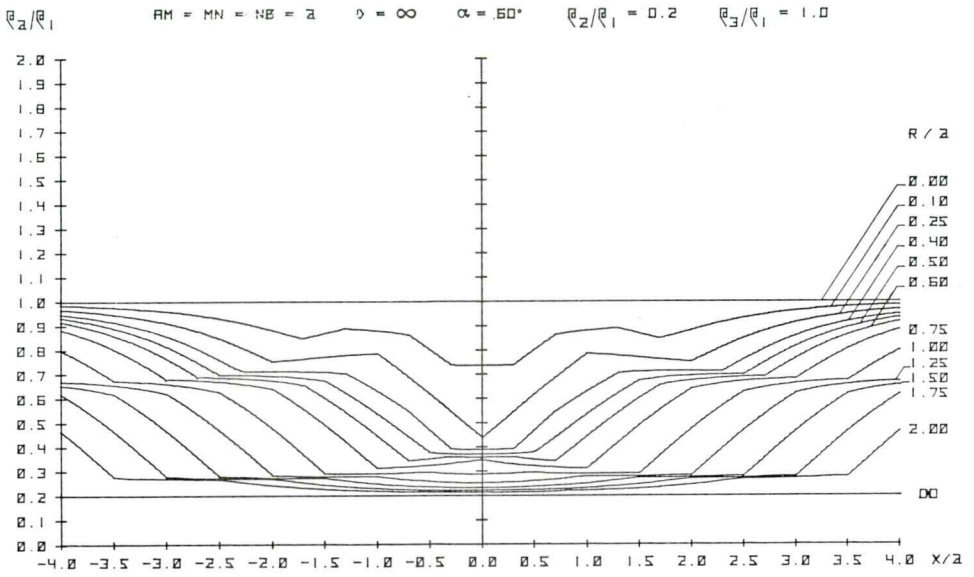


Fig. 48. Resistivity type curves over vertical dike
 Sl. 48. Modelne krivulje vertikalne plošče

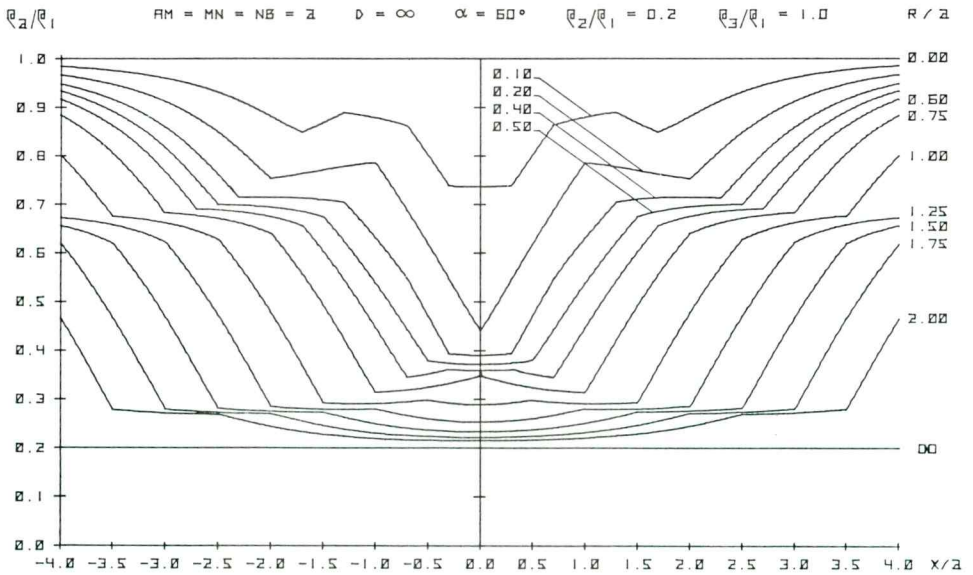


Fig. 48 a. Resistivity type curves over vertical dike
 Sl. 48 a. Modelne krivulje vertikalne plošče

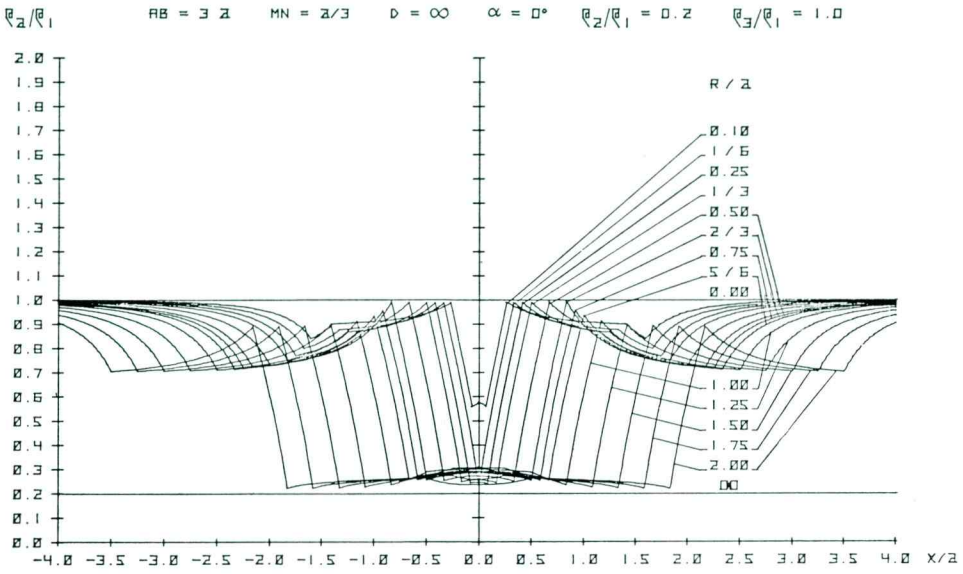


Fig. 49. Resistivity type curves over vertical dike
Sl. 49. Modelne krivulje vertikalne plošče

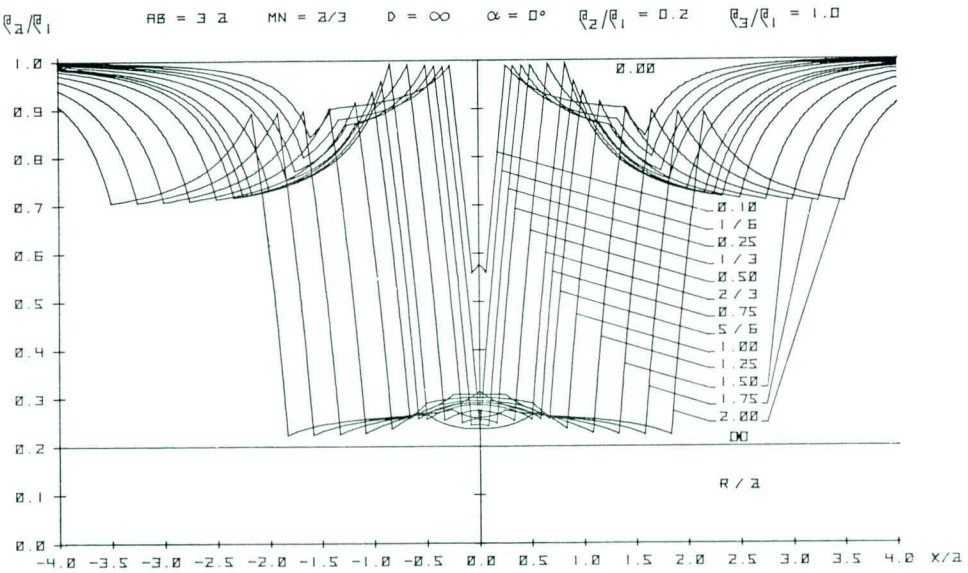


Fig. 49 a. Resistivity type curves over vertical dike
Sl. 49 a. Modelne krivulje vertikalne plošče

Table 1. List of resistivity type curves
Tabela 1. Seznam modelnih krivulj

Sl. Fig.	MODEL MODEL	RAZVRSTITEV ARRAY	FUNKCIJA FUNCTION	IZBRANE VREDNOSTI FIXED VALUES	PARAMETER DRUŽINE KRIVULJ SET PARAMETER VALUES
13	Polkrogla Hemisphere	Wenner	$\rho_a/\rho_1 = f(x/a)$	$\gamma = 0$	$\rho_2/\rho_1 = 0$ $R/a = 0.1, 0.25, 0.4, 0.5, 0.6, 0.75, 1, 1.25, 1.5, 2$
14	"	"	"	"	0.2 "
15	"	"	"	"	0.5 "
16	"	"	"	R	0 "
17	"	"	"	"	0.2 "
18	"	"	"	"	0.5 0.25, 0.5, 0.75, 1, 1.5, 2
19	"	"	"	0	$R/a = 0.25$ $\rho_2/\rho_1 = 0, 0.1, 0.2, 0.3, 0.5, 0.7$
20	"	"	"	0	0.5 "
21	"	"	"	"	0.75 "
22	"	"	"	R	0.25 0, 0.2, 0.5
23	"	"	"	"	0.5 0, 0.1, 0.2, 0.3, 0.5, 0.7
24	"	"	"	"	0.75 "
25	"	"	"	$R/a = 0.25$	$\rho_1/\rho_2 = 0$ $\gamma/R = 0, 0.6, 1, 1.6$
26	"	"	"	"	0.2 "
27	"	"	"	$R/a = 0.25$	$\rho_2/\rho_1 = 0.5$ $\gamma/R = 0, 1$
28	"	"	"	0.5	0 0, 0.4, 0.6, 0.8, 1, 1.2, 1.6, 2
29	"	"	"	"	0.2 "
30	"	"	"	"	0.5 0, 0.6, 1, 1.6
31	"	"	"	0.75	0 0, 0.4, 0.6, 0.8, 1, 1.2, 1.6, 2
32	"	"	"	"	0.2 "
33	"	"	"	"	0.5 0, 0.6, 1, 1.6
34	"	Schlumberger	"	$\gamma = 0$	0.2 $R/a = 0.1, 1/6, 0.25, 1/3, 0.5, 2/3, 0.75, 5/6, 1, 1.25, 1.50, 1.75, 2$

nadaljevanje		continued					
Sl. Fig.	MODEL MODEL	RAZVRSTITEV ARRAY	FUNKCIJA FUNCTION	IZBRANE VREDNOSTI FIXED VALUES		PARAMETER DRUŽINE KRIVULJ SET PARAMETER VALUES	
35	Polkrogla Hemisphere	Wenner	$\rho_a/\rho_1 = f(a/R)$	$x = 0$	$y = 0$	$\rho_2/\rho_1 = 0, 0.1, 0.2, 0.3, 0.4, 0.5, 0.6, 0.7, 0.8, 0.9$	
36	"	Schlumberger	"	"	"	"	
37	"	Wenner	$\rho_{\min}/\rho_{\max} = f(a/R)$	—	"	"	
38	"	Schlumberger	"	—	"	" (in and 0.01)	
39	"	Wenner	$\rho_a/\rho_1 = f(R/a)$	$x = 0$	"	"	
40	"	Schlumberger	$\rho_a/\rho_1 = f(R/a)$	$x = 0$	$y = 0$	$\rho_2/\rho_1 = 0, 0.1, 0.2, 0.3, 0.4, 0.5, 0.6, 0.7, 0.8, 0.9$	
41	"	Wenner	$\rho_{\min}/\rho_{\max} = F(R/a)$	—	"	"	
42	"	Schlumberger	"	—	"	"	
43	"	Wenner	$\rho_a/\rho_1 = f(y/a)$	$x = 0$	$\rho_2/\rho_1 = 0.2$	$R/a = 0.25, 0.4, 0.5, 0.6, 0.75, 1, 1.25, 1.5, 1.75, 2$	
44	"	"	$\rho_a/\rho_1 = f(R/a)$	"	"	$y/a = 0, 0.5, 0.75, 1, 1.25, 1.5, 2$	
45	"	"	$\rho_a/\rho_1 = f(\rho_2/\rho_1)$	"	—	$(R/a, y/a) = 0, 0.25) \dots$	
46 46a	Ploščica Dike	"	$\rho_a/\rho_1 = f(x/a)$	$\alpha = 0$	$\rho_2/\rho_1 = 0.2$	$\rho_3/\rho_1 = 1$	$R/a = 0.1, 0.25, 0.4, 0.5, 0.6, 0.75, 1, 1.25, 1.5, 1.75, 2$
47 47a	"	"	"	"	"	0.6	"
48 48a	"	"	"	60°	"	1	"
49 49a	"	Schlumberger	"	0	"	"	"
50	Polsferoidi Hemispheroids	Wenner	"	$y = 0$	$R/a = 0.5$	$\alpha = 0$	$D/R = 0.1, 0.5, 1, 2, 4$ ∞

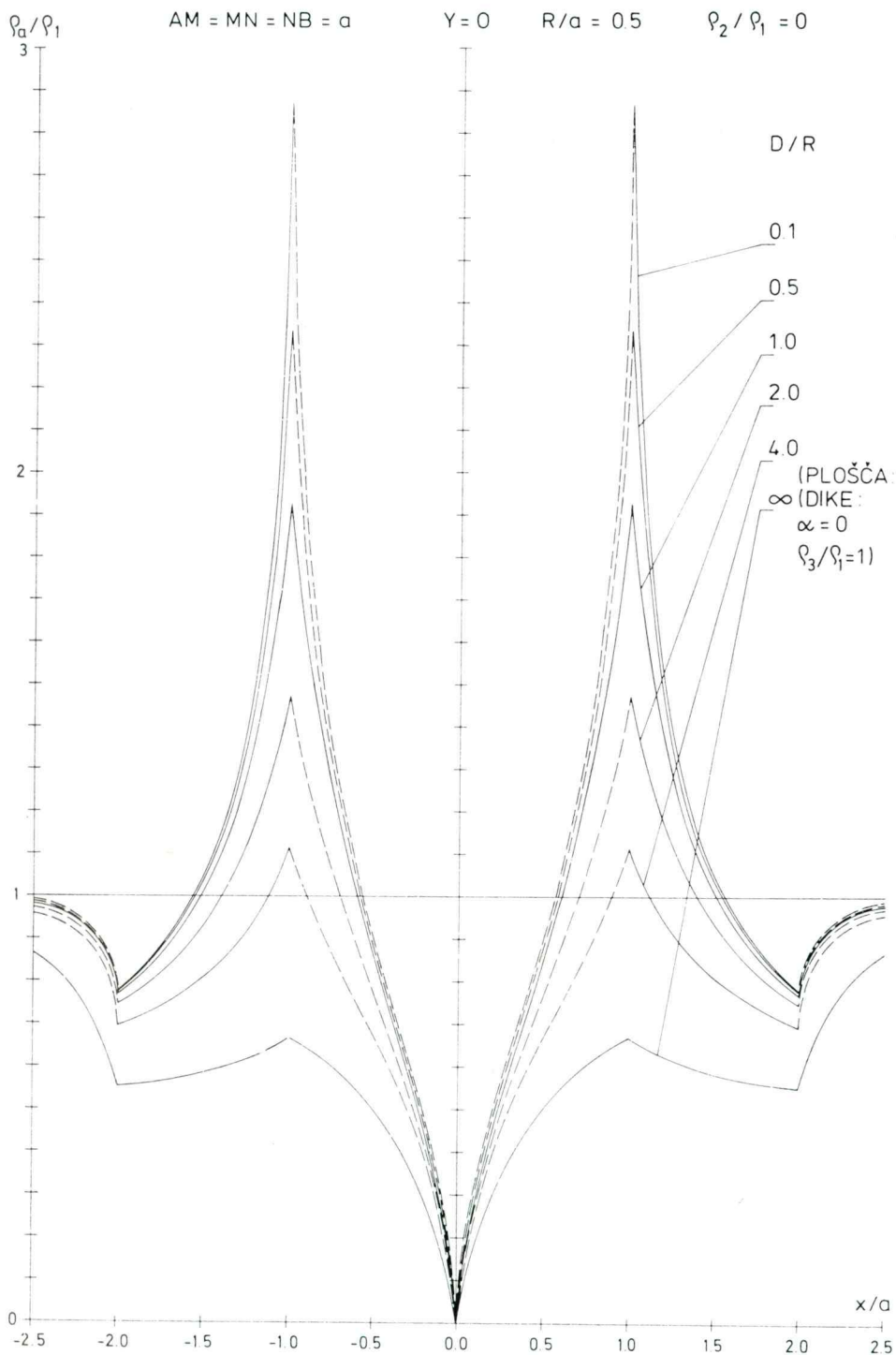


Fig. 50. Resistivity type curves over hemisphere, oblate and prolate hemispheroid and vertical dike. Solid lines — computed, dashed sections — interpolated

Sl. 50. Modelne krivulje polkrogle, sploščenega in podaljšanega polsferoida in vertikalne plošče. Neprekinjeni odseki krivulj so izračunani, črtkani pa interpolirani

2.3. Analysis of resistivity type curves

From a total of 38 diagrams there are 27 sets illustrating the theoretical horizontal resistivity profiles $\varrho_a/\varrho_1 = f(x/a)$. Resistivity profiles over the body are characterized by break points. They appear where one or two electrodes traverse the body and the country rock. In the symmetrical AMNB electrode array the turning points are at:

hemispheriod	dike
$x_1 = \pm \left \frac{\overline{MN}}{2} - \sqrt{R^2 - y^2} \right $	$x_1 = \pm \left \frac{\overline{MN}}{2} - \frac{R}{\cos \alpha} \right $
$x_2 = \pm \left \frac{\overline{MN}}{2} + \sqrt{R^2 - y^2} \right $	$x_2 = \pm \left(\frac{\overline{MN}}{2} + \frac{R}{\cos \alpha} \right)$
$x_3 = \pm \left \frac{\overline{AB}}{2} - \sqrt{R^2 - y^2} \right $	$x_3 = \pm \left \frac{\overline{AB}}{2} - \frac{R}{\cos \alpha} \right $
$x_4 = \pm \left(\frac{\overline{AB}}{2} + \sqrt{R^2 - y^2} \right)$	$x_4 = \pm \left(\frac{\overline{AB}}{2} + \frac{R}{\cos \alpha} \right)$

The hemisphere model curves show how the amplitude and the shape of the anomaly are influenced by parameters y/R , R/a and ϱ_2/ϱ_1 . The anomalies decrease as the body resistivities advance towards that of the country rock, as well as with the growing distance of the traverse from the center of the body, i.e. with the increase of y/R or y/a . This relationship is self-evident. Nevertheless, the decrement of the anomaly, as well as the changing of its shape, are important, as can be observed in the diagrams.

The anomaly at point ($x = 0$, $y = 0$) as a function of y/a and ϱ_2/ϱ_1 is shown in figs. 43 and 45. By increasing the distance of the traverse from the center of the body of radius $R > \overline{MN}/2$, the change in the anomaly at point (0,0) is practically negligible up to $y = \sqrt{R^2 - (\overline{MN}/2)^2}$ (it increases slightly). At this point the potential electrodes leave the body and, further on, the anomaly decreases with considerable speed (fig. 43). With the increased ratio ϱ_2/ϱ_1 , the anomaly decreases rather rapidly (fig. 45).

On the other hand, the relation of the anomaly to the radius of the hemisphere has proved to be somehow more complicated. Fig. 44 illustrates the relation of $\varrho_a/\varrho_1 = f(R/a)$ at point $x = 0$ for different traverse positions. Where R/a is augmented the anomaly increases fast, thus reaching

$$R = \sqrt{(\overline{MN}/2)^2 + y^2}$$

at this point the potential electrodes are at the very edge of the body.

A further augmentation of R/a does not change considerably the anomaly much (it increases slightly as y is increased) until the point where $R = \sqrt{(\overline{AB}/2)^2 + y^2}$ when the current electrodes enter the body. From this point on, the anomaly increases slightly again. Fig. 39 illustrates the anomaly

at point $(x = 0, y = 0)$ as a function of the radius of the hemisphere for different values of resistivity of the body.

The evaluation of the anomaly at point $(0,0)$ reveals but some of the characteristics relative to resistivity profiles; none of the remaining characteristics emerge before the entire anomaly is examined. Diagrams shown in figs. 13, 14 and 15 point to rather important characteristics: the ratio ϱ_a/ϱ_1 , reaches its maximum at a defined R/a value. However, at higher and lower values of R/a , the anomaly amplitude is lower. The maximum value of ϱ_a/ϱ_1 corresponds to the radius of the sphere $R = \overline{AM}/2 = \overline{NB}/2$; in the Wenner array this radius equals $0.5 a$. When ϱ_a/ϱ_1 is at its maximum in the equation (3) then $x_2 = x_3$. Accordingly, the highest sensitivity of resistivity profiling refers to the case where the body radius of $R = \overline{AM}/2 = \overline{NB}/2$ (except for high R/a values). The ratio of the minimum and maximum apparent resistivity values on the anomaly may be regarded as the measure of sensitivity. Fig. 41 presents this ratio as the function of R/a for different values ϱ_2/ϱ_1 . At smaller R/a values, the minimum representation on the curves is at $R/a = 0.5$

The question of sensitivity may be viewed also from another point of view: Which electrode spacing in the Wenner array is most appropriate for resistivity profiling? Fig. 35 illustrates the dependence of the anomaly on the array dimension at point $(0,0)$. The highest sensitivity point can be reached in closely spaced arrays which are not practicable because of the heterogeneity of the ground and rather low depth penetration. The most appropriate values are $\overline{AB}/2 = 3 a/2 > R$. However, referring to fig. 35 there ought to be $a/R \leq 2$. The most appropriate array dimension may be determined precisely by means of curves $\varrho_{min}/\varrho_{max} = f(a/R)$ (see fig. 37).

These curves demonstrate that the most useful value is $a/R = 2$ (or $R/a = 0.5$). An upward deviation of this value is more favorable than the opposite. This is valid especially for traverses running at a distance from the center of the body; the optimum array length is $a/R = 2 \sqrt{1 - (y/R)^2}$ in this case.

Accordingly, the Wenner array may be compared to the Schlumberger array, as presented in the diagrams (figs. 14 and 35); fig. 35 illustrates the model curves for an inexact Schlumberger array — $AB/MN = 9$. For easier comparison, the dimension a of the Wenner array has also been introduced in this diagram, although in the Schlumberger array the parameter AB or $AB/2$ (for $AB = 3 a$) is usually applied. As expected, the Schlumberger array proved to be more sensitive to the inhomogeneities than Wenner's. In addition, the Schlumberger anomalies display a useful characteristic: they are limited by rather steep lines (in an exact Schlumberger array these "limits" are vertical).

In any arbitrary inexact Schlumberger array, the maximum ϱ_a/ϱ_1 value pertains to the body, the radius of which varies between $R = AB/6 = 0.5 a$ (in the Wenner array) and $R = AB/4 = 0.75 a$ (in an exact Schlumberger array); in our case this is $R = 2 \overline{AB}/9 = 2 a/3$. The characteristics of the Schlumberger array are evident also from figs. 36, 38, 40 and 42. Also in the Schlumberger array the function $\varrho_{min}/\varrho_{max} = f(a/R)$ or $\varrho_{min}/\varrho_{max} = f(R/a)$ reaches its minimum at certain R/a ; at this value the set of $\varrho_a/\varrho_1 = f(x/a)$ shows maximum point.

The sensitivity of the Schlumberger array increases with the growing ratio $\overline{AB/MN}$, and has an advantage over the Wenner array. It has, however, a weak point since it is susceptible to small bodies and inhomogeneities, both features of limited interest. The anomalies they provoke burden the recorded resistivity profiles and inhibit the interpretation. Accordingly the Wenner array serves as a sort of "high-cut filter" suppressing the influence of smaller bodies and heterogeneities on the resistivity profile.

Considering the entire anomaly, one could conclude that the equivalence is of no importance because of the various forms of the anomalies. However, its full significance at point $x = 0$ is evident, as is well illustrated in figs. 43 and 44, and particularly in fig. 45. For every curve $\rho_a/\rho_1 = f(\rho_2/\rho_1)$ at $x = 0$, there is an unlimited number of pairs $(R/a, y/a)$. The equivalence is above all conditioned by the low density of observation points on the profile; its domain increases correspondingly even if the entire anomaly is taken into consideration.

Four characteristic sets of curves (figs. 46 to 49 and 46a to 49a) are given for the vertical dike. The set of curves as presented in fig. 46 may be compared to the set shown in fig. 14, and the curves of fig. 49 with the curves of fig. 34. An apparently strange characteristic immediately emerges. The anomalies at certain R/a values pertaining to the hemisphere, are better expressed than the corresponding anomalies of the dike, because of the increase of the apparent resistivity at $x = \overline{MN}/2 + R$ in the case of the hemisphere.

Fig. 47 presents a set of curves for different resistivities on both sides of the dike, whereas fig. 48 illustrates the anomalies of the traverse running obliquely across the dike. Where the dike is narrow, the anomalies are somewhat higher for oblique traverses compared to the corresponding anomalies of perpendicular traverses. It has been discovered that the anomalies of the hemisphere are at times better expressed if compared to the corresponding anomalies of the dike. This observation is better illustrated in fig. 50 which shows the anomalies of the prolate and oblate hemispheroids beside the anomalies of the hemisphere and dike. The diagram thus expresses an important paradox: the thinner the body, the higher the anomaly. This phenomenon is especially relevant where the body has very low resistivity and at appropriate geometric parameters. The explanation of the paradox might be found in the fact that in such cases, one current electrode and one potential electrode are connected by a good conductor, whereas the third and the fourth electrodes are isolated from the first two, as well as from each other. In practice, however, this phenomenon may cause inconvenience since the anomalies of insignificant bodies could be interpreted as the reflection of larger geological features. In order to avoid the misinterpretation, it is necessary to examine the shape of the anomalies, as well as the values of the apparent resistivity, thoroughly.

Referring to the geophysical investigation of bauxite deposits in Istria, some questions arose. An attempt is made here to answer two of them: the first concerns the choice of the array type, and the second, the elimination of the anomalies at the sites featuring a comparatively small thickness of low-resistivity surface layer. With reference to the Wenner array, the choice was correct because it was less sensitive to small inhomogeneities. The Schlumberger array on the other hand, would register greater number of anomalies and its

results would be consequently more difficult to interpret. The paradox discussed, as illustrated in fig. 50, points to the apparently justified decision related to the second question, although insufficient attention has been given to the shape of the anomalies and to the values of apparent resistivity.

3. The quantitative processing of anomalies

3.1. Numerical proceedings

In the first chapter it was supposed that the apparent resistivity anomalies arose either from the Eocene cover of the bauxite or from both, the hanging wall and bauxite together. This supposition led to the hemispheroid model and even to the dike. The comparison of field and model anomalies for the hemispheroid and for the dike confirms their suitability and justifies the quantitative verification.

Seven locations of different depths and dimensions of the bauxite bodies were selected for quantitative processing. On the locations bauxite is present at a depth of between 11.5 m (locality 20) and 54 m (locality 18). The thickness of the penetrated bauxite layers varies between 2 m (locality 61) and 19.5 m (locality 109). All the anomalies are sharp, regardless of the depth and the size of the bauxite body, confirming thus the assumption that the bauxite body does not contribute much to the lowering of the apparent resistivity in geoelectrical profile.

The numerical processing of the anomalies is based on the trial-and-error process, derived from the supposed model, the hemispheroid and the dike in our case. The corresponding equations have already been quoted in the previous chapter. The mathematical proceeding is given in the flow chart (fig. 51), where the root mean square error of fit RMS is expressed by the equation:

$$RMS = \sqrt{\frac{1}{N} \sum_{i=1}^N \left(\frac{\rho_{im} - \rho_{it}}{\rho_{im}} \right)^2}$$

and the meaning of symbols is as follows:

RMS = root mean square error

ρ_{im} = observed apparent resistivity at observation point "i"

ρ_{it} = theoretical apparent resistivity at observation point "i"

N = number of observations in a selected section of the resistivity profile.

In the case of the hemisphere, the iteration comprises the following parameters: resistivity ratio of the body and the country rock (ρ_2/ρ_1), radius (R), the position of the hemispheroid center on axis x (x_0) and the position of the center on the axis y (y_0). In the case of the dike, the procedure involves the ratio of the body resistivity to both parts of the country rock (ρ_2/ρ_1 , ρ_3/ρ_1), the thickness of the dike ($2R$), the position of the dike axis on the traverse (x_0) and the direction of the traverse to the strike of the dike (fig. 51).

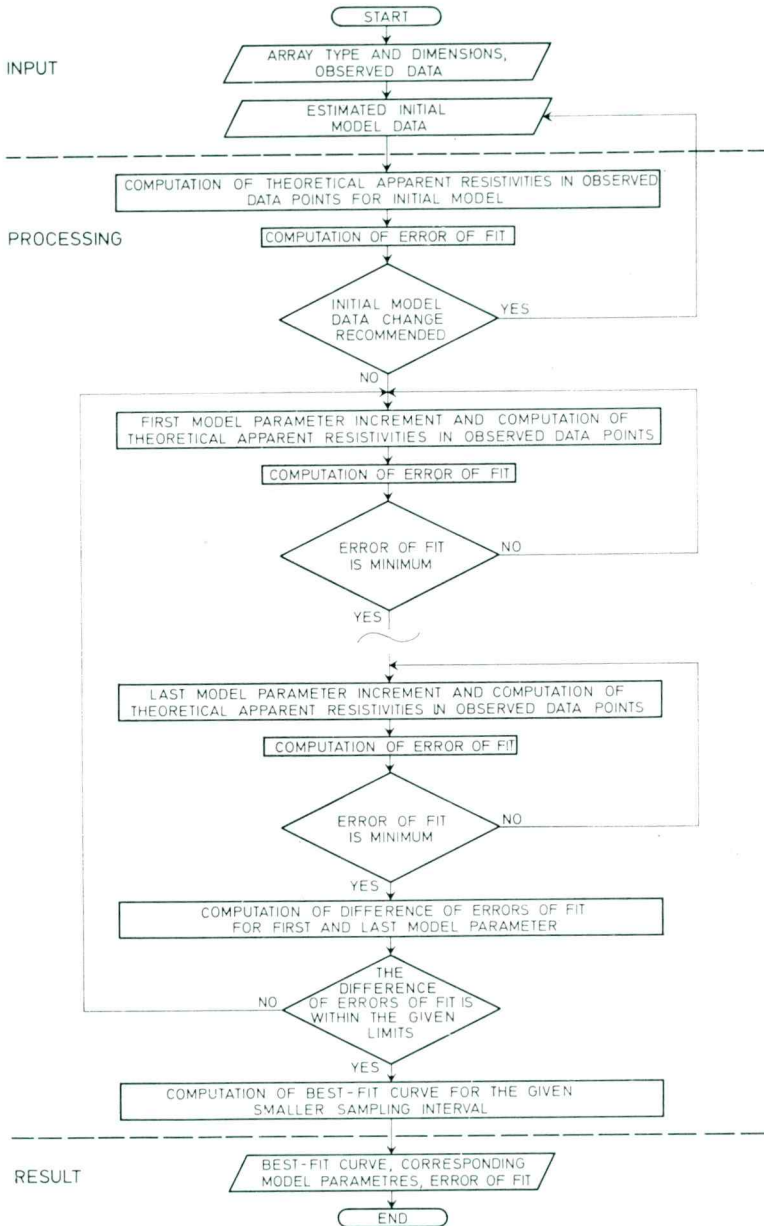
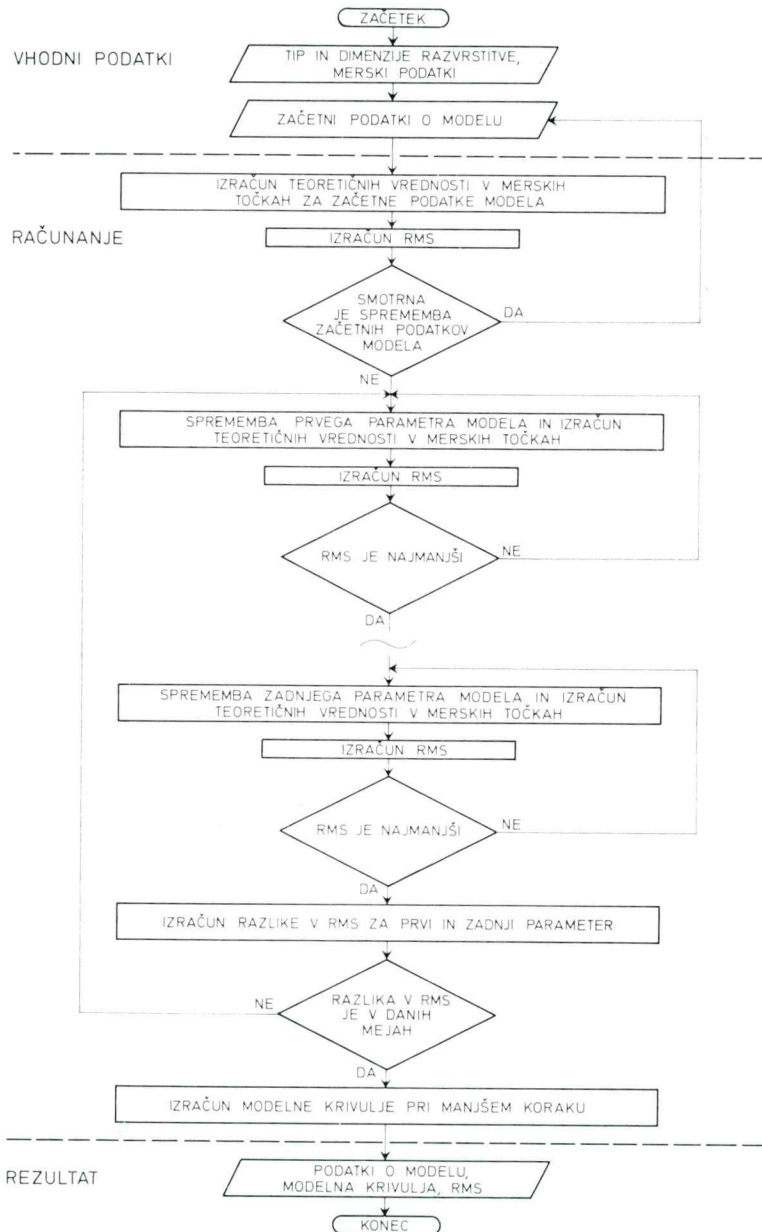


Fig. 51. Flow chart of anomaly processing



Sl. 51. Diagram toka numerične obdelave anomalije

3.2 Results of quantitative processing

The numerical procedure described was applied for the anomalies of locations Nos. 10, 18, 20, 26, 61, 105 and 109 as well as for the test location anomalies. The processing data are presented in figs. 52 to 70. It is evident from the diagrams that in the case of most of the profiles, the model curves fit the measured values quite satisfactorily. The resulting values of all model parameters are listed in tables 2 and 3, together with the corresponding *RMS* values (x_0 and y being the coordinates of the body center relative to the traverse). At the test locality, various electrode arrays make the parameter values more or less different. The differences in coordinates of the body center are comparatively small (except the value of y in the array $a = 10$ m), which is a promising point regarding the location of the drilling sites. Somewhat less consistent are the values of body dimensions, particularly for different models — the hemisphere and the dike. It should be mentioned that a smaller diameter, in the case of the dike, is involved in the shape of an anomaly and most probably in an inclined profile direction to the strike of the dike. Parameters pertaining to the same model vary, due to the horizontal and vertical inhomogeneities of limestone, the fissuring and karstification and the variable thickness of the low-resistivity surface layer. The treated models must therefore be regarded as rough approximations of field conditions only. The horizontal inhomogeneity is evident in the apparent resistivity profile, whereas the vertical inhomogeneities are shown in the comparison of profiles of different depth penetrations. Fig. 2 (as well as fig. 9) clearly illustrates the increase of the average apparent resistivity with the increase in depth of penetration, which means the increase of resistivity in relation to the depth. Observation of the values in table 2 shows the same fact, which is evident from the course of the value ρ_1 . Resistivity increases in proportion to depth, owing to a lesser degree of fissuring and karstification. Moreover, the apparent resistivity increases as the current electrodes are separated; the increase is also due to the weakening in influence of the low-resistivity surface layer. This fact is reflected, in the case of simple models, in somewhat higher resistivities of the body and country rock.

The *RMS* values at the test site show that the theoretical curves differ from the observed anomalies by an average of 3 (fig. 57) to 10 per cent (fig. 59). This does not imply, however, such a close similarity between the models and the geological formations. Nevertheless, the values under 10 per cent may be considered as very favorable, whereas the somewhat higher values are only satisfactory.

Because of the influence of other bodies as well as the inhomogeneities in general, it is not advisable to process quantitatively longer sections of the resistivity profiles. This is illustrated by the $a = 10$ m resistivity profile of the test location. In the section between 0 and 70 m of the profile, the *RMS* value amounts to 0.091 for the hemisphere and the dike, whereas in the section between 0 and 60 m the value for the hemisphere is 0.84 and 0.032 for the dike respectively. On the other hand, the model and field anomalies of the Wenner arrays with $a = 20$ m and $a = 30$ m fit very well, though the differences of calculated geometrical parameters are comparatively large. The processing of the test location anomaly may be used for the estimation of the accuracy of the

calculated model parameters. The position and the size of the body are important in this respect, and perhaps the strike of the dike as well. These parameters enable the setting of the exploratory drillholes.

For the rest of the locations, the theoretical curves generally fit the observed anomalies (figs. 60 to 70) even better. A summary of the processing data is presented in table 3. For some locations the parameters have been estimated in two ways.

The anomalies of two crossed traverses were evaluated at location No. 10, the calculated values for the body radius and for the body and country rock resistivities differing considerably. The conclusion is that the ground settlement is elongated in the direction of traverse 1b, thus explaining a somewhat higher apparent resistivity in this direction.

The values of the same parameters for two different arrays may be compared at location No. 20. More or less identical values for the position of the body were obtained in both cases (relatively remarkable variations in y are not of any particular significance, the absolute values of y being low), whereas the variation in radii is obvious. Somewhat greater resistivity values in the case of deeper penetration have already been given.

The anomalies at locations Nos. 105 and 109 are interpreted by two models: the hemisphere and the dike. Here, too, the identical position of the bodies has been calculated and the dimensions of the bodies do not vary much. On the other hand the variations in resistivities are considerable. The real value may therefore be expected between the two values, i.e. between the value for the hemisphere and the value for the dike. With reference to the smaller *RMS* value in the case of the dike, it might be concluded that the corresponding resistivities are closer to the real values than the corresponding values of the hemisphere.

Rather small *RMS* values show that model and field anomalies match well. At location No. 26 (fig. 65) there is a satisfactory matching for a rather long section of the resistivity profile, so enabling the presentation of the entire anomaly. A remarkable *RMS* value was obtained at location No. 109 for the hemispheroid model. For the dike, the *RMS* value is halved, this fact pointing to an elongated settlement. However, the fact that the theoretical and observed anomalies match, because of the equivalence, does not mean that the model corresponds well to the geological structure. Rough models should nevertheless be appreciated if the inhomogeneity of the karst is taken into consideration.

The sensitivity of the applied electrode array can be estimated from the ratio of the body radius and of the electrode spacing in the Wenner array, as shown in tables 2 and 3. For the test location, the R/a values are somewhat more dispersed, whereas for the rest of locations, the R/a is between 0.4 and 0.6, or at least very close to these values. As stated in the previous chapters, the electrode spacing gives optimum sensitivity in the Wenner array at $R/a = 0.5$. Accordingly, the most appropriate spacing was observed for the examination of bauxite deposits.

The largest bauxite body was found at location No. 109. Because of its relatively shallow depth, the direct model anomalies were calculated for this location. Figure 71 shows that the anomaly of a perfect conductive sphere is extremely small. Thus it follows that no direct geophysical model is available for the resistivity survey of the Istrian bauxite deposits.

Table 2. Test location. Review of results of processing resistivity profiles
 Tabela 2. Poskusna lokacija. Pregled rezultatov numerične obdelave geoelektričnih anomalij

Sl. Fig.	RAZVRSTITEV ARRAY	PROFIL PROFILE (m)	a MN/AB (m)	MODEL MODEL	x_o (m)	y (m)	R (m)	R/a	α (°)	ρ_1 ($\Omega \cdot m$)	ρ_2 ($\Omega \cdot m$)	ρ_3 ($\Omega \cdot m$)	RMS
51	Wenner	0-70	10	Polkrogla Hemisphere	30.9	8.1	11.7	1.17	-	390	120	-	0.091
52	"	0-70	10	Plošča Dike	31.4	-	8.0	0.80	0	390	160	410	0.091
53	"	0-60	10	Polkrogla Hemisphere	31.3	7.0	11.6	1.17	-	400	120	-	0.084
54	"	0-60	10	Plošča Dike	31.4	-	7.9	0.79	16.6	400	150	470	0.032
55	"	0-70	20	Polkrogla Hemisphere	31.5	0.5	15.3	0.77	-	690	220	-	0.043
56	"	0-70	30	"	28.0	0.3	12.4	0.41	-	880	240	-	0.028
57	"	0-70	40	"	27.2	0.5	13.8	0.35	-	1120	240	-	0.081
58	Schlumberger	5-65	10/70	"	28.4	1.3	16.5	(0.71)	-	1060	330	-	0.098

Table 3. Other locations. Review of results of processing resistivity profiles
 Tabela 3. Ostale lokacije. Pregled rezultatov numerične obdelave geoelektričnih anomalij

Sl. Fig.	Lokacija Location	Profil Profile	a (m)	Model Model	x_0 (m)	y (m)	R (m)	R/a	α ($^\circ$)	ρ_1 (om.m)	ρ_2 (om.m)	ρ_3 (om.m)	RMS
59	10	1b	30	Polkrogla Hemisphere	111.4	0.1	18.4	0.61	-	1050	450	-	0.054
60	10	3a	30	"	255.5	0.4	12.9	0.43	-	650	180	-	0.076
61	18	13	30	"	277.5	0.2	12.7	0.42	-	1090	360	-	0.028
62	20	11	30	"	265.9	0.1	25.4	0.85	-	1080	590	-	0.013
63	20	11	40	"	265.0	0.2	30.1	1.00	-	1200	610	-	0.041
64	26	15a	30	"	118.2	0.7	17.5	0.58	-	620	180	-	0.049
65	61	33a	30	"	92.2	1.1	14.0	0.47	-	690	270	-	0.048
66	105	56	30	"	856.8	1.4	11.9	0.40	-	490	90	-	0.078
67	105	56	30	Ploščča Dike	859.3	-	12.6	0.42	16.3	710	130	770	0.064
68	109	69	30	Polkrogla Hemisphere	562.0	6.4	19.1	0.64	-	480	70	-	0.126
69	109	69	30	Ploščča Dike	562.0	-	17.5	0.58	0	790	80	850	0.066

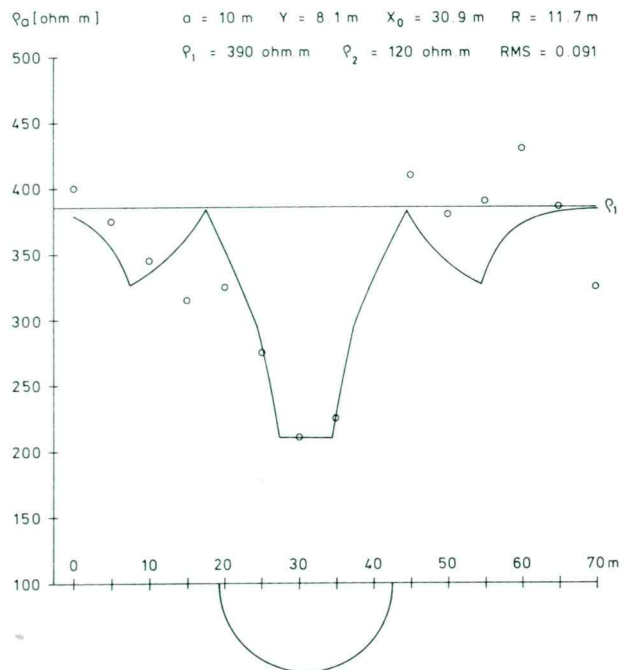


Fig. 52. Test location, $a = 10$ m. Observed and best fit hemisphere model data

Sl. 52. Poskusna lokacija, $a = 10$ m. Rezultat numerične obdelave anomalije z modelom polkrogle

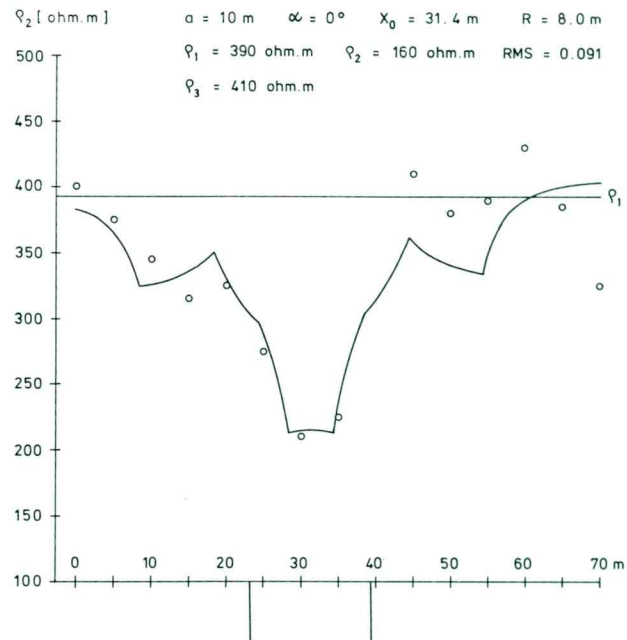


Fig. 53. Test location, $a = 10$ m. Observed and best fit vertical dike model data

Sl. 53. Poskusna lokacija, $a = 10$ m. Rezultat numerične obdelave anomalije z modelom vertikalne plošče

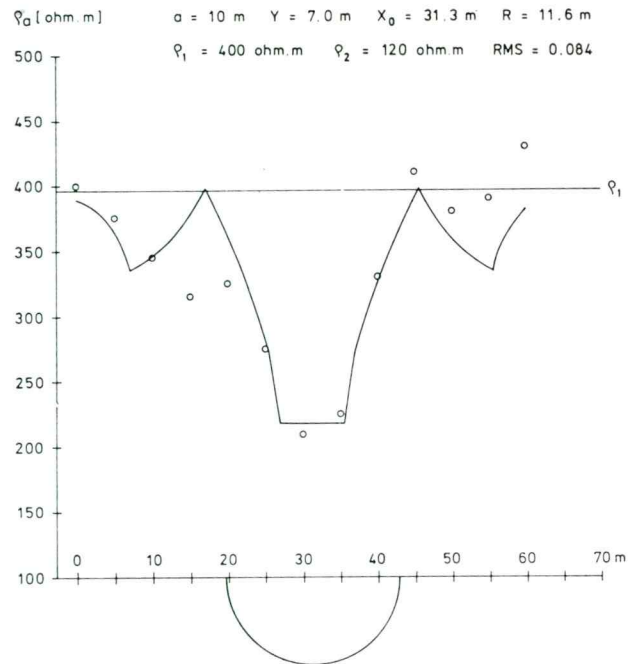


Fig. 54. Test location, $a = 10$ m. Observed and best fit hemisphere model data

Sl. 54. Poskusna lokacija, $a = 10$ m. Rezultat numerične obdelave anomalije z modelom polkrogle

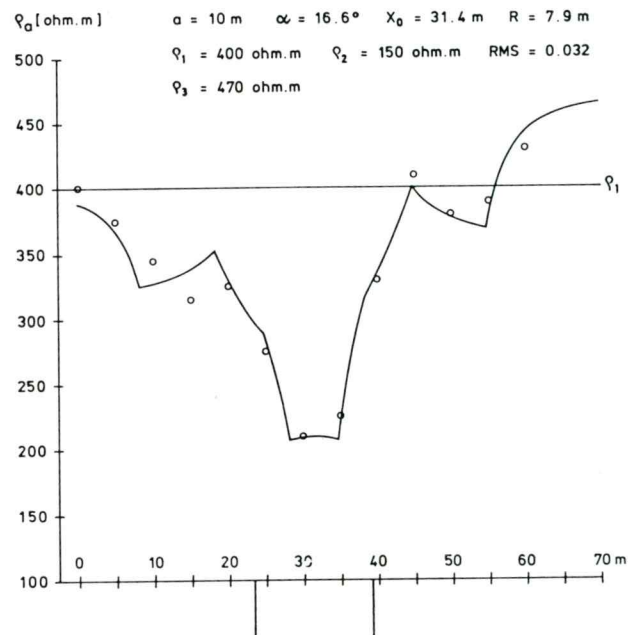


Fig. 55. Test location, $a = 10$ m. Observed and best fit vertical dike model data

Sl. 55. Poskusna lokacija, $a = 10$ m. Rezultat numerične obdelave anomalije z modelom vertikalne plošče

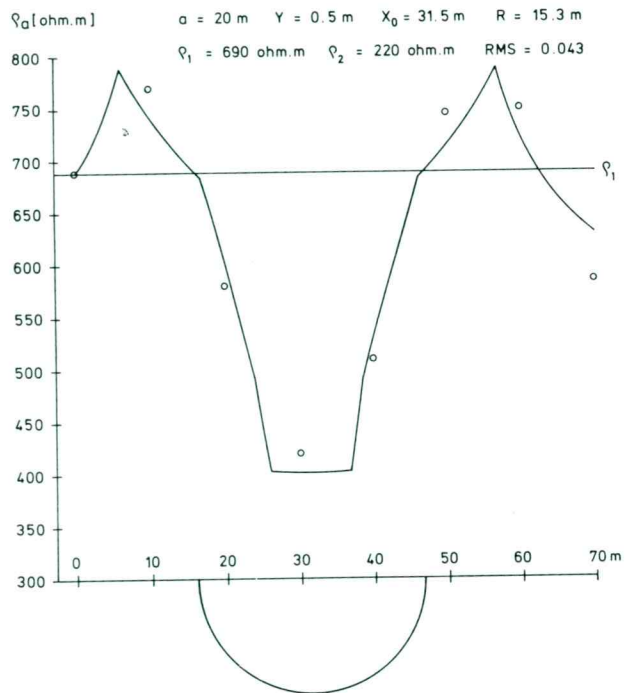


Fig. 56. Test location, $a = 20 \text{ m}$. Observed and best fit hemisphere model data

Sl. 56. Poskusna lokacija, $a = 20 \text{ m}$. Rezultat numerične obdelave anomalije z modelom polkrogle

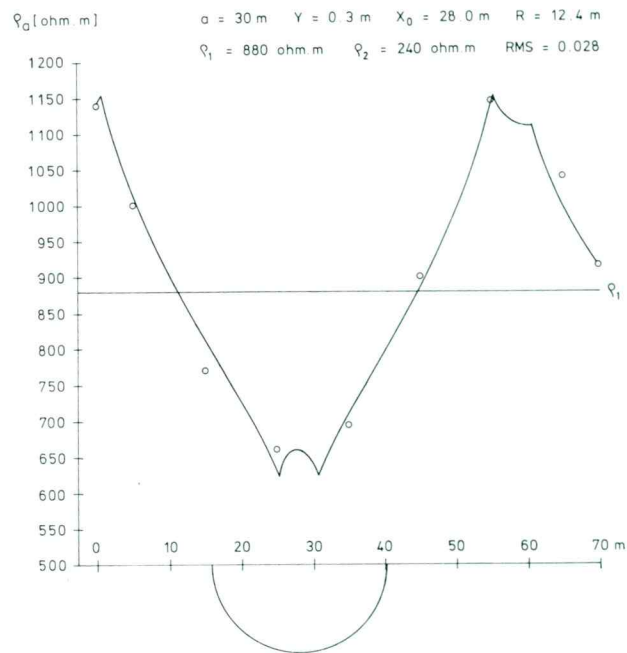


Fig. 57. Test location, $a = 30 \text{ m}$. Observed and best fit hemisphere model data

Sl. 57. Poskusna lokacija, $a = 30 \text{ m}$. Rezultat numerične obdelave anomalije z modelom polkrogle

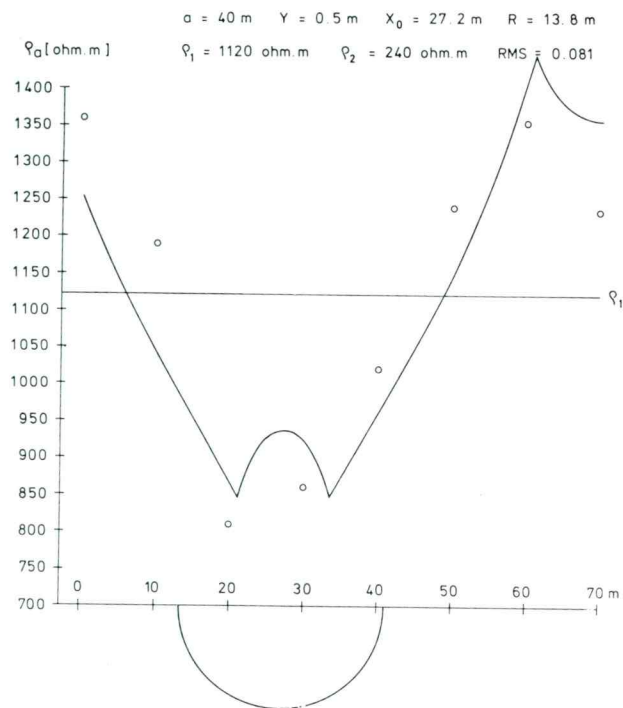


Fig. 58. Test location, $a = 40 \text{ m}$. Observed and best fit hemisphere model data

Sl. 58. Poskusna lokacija, $a = 40 \text{ m}$. Rezultat numerične obdelave anomalije z modelom polkrogle

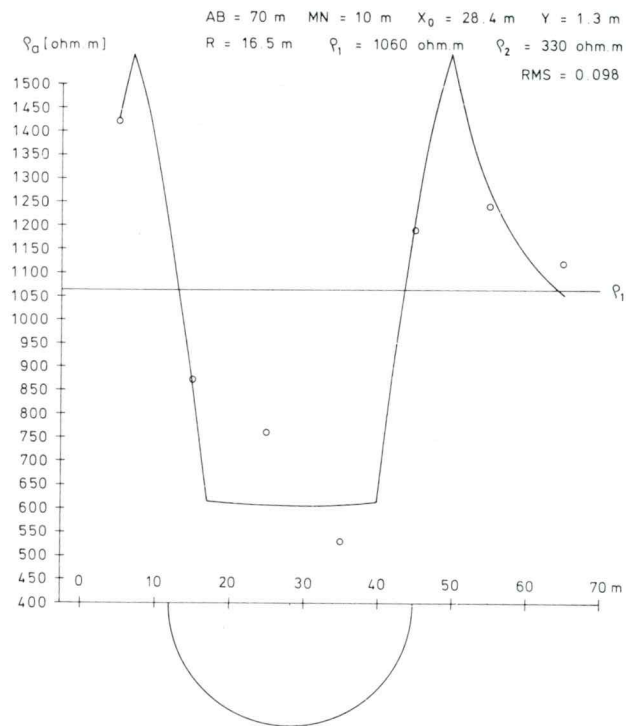


Fig. 59. Test location, $AB = 70 \text{ m}$, $MN = 10 \text{ m}$. Observed and best fit hemisphere model data

Sl. 59. Poskusna lokacija, $AB = 70 \text{ m}$, $MN = 10 \text{ m}$. Rezultat numerične obdelave anomalije z modelom polkrogle

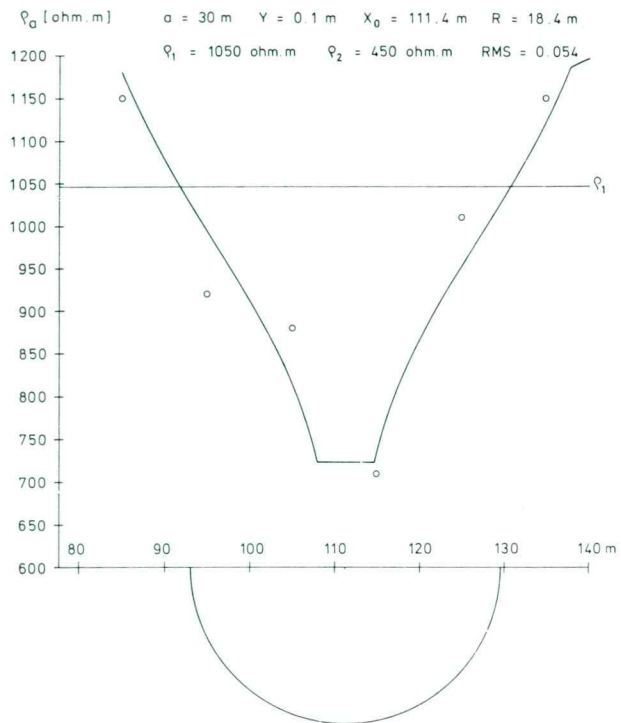


Fig. 60. Location 10, profile P-1 b. Observed and best fit hemisphere model data

Sl. 60. Lokacija 10, profil P-1 b. Rezultat numerične obdelave anomalije z modelom polkrogle

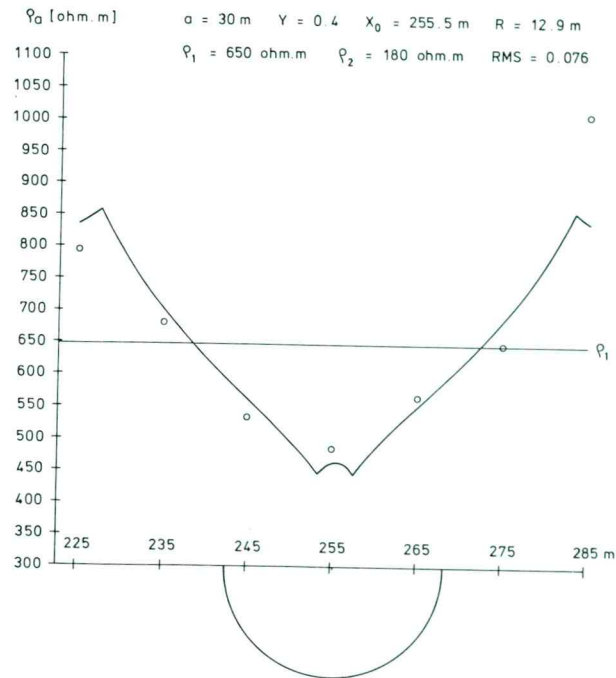


Fig. 61. Location 10, profile P-3 a. Observed and best fit hemisphere model data

Sl. 61. Lokacija 10, profil P-3 a. Rezultat numerične obdelave anomalije z modelom polkrogle

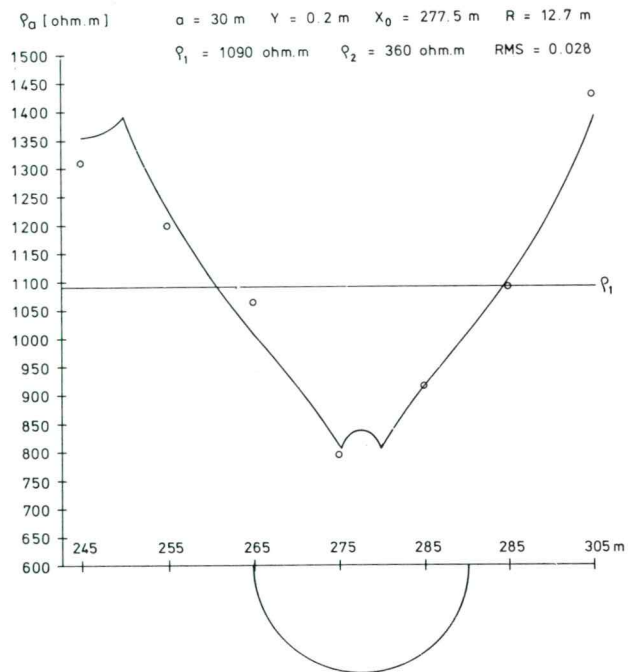


Fig. 62 .Location 18, profile P-13. Observed and best fit hemisphere model data

Sl. 62. Lokacija 18, profil P-13. Rezultat numerične obdelave anomalije z modelom polkrogle

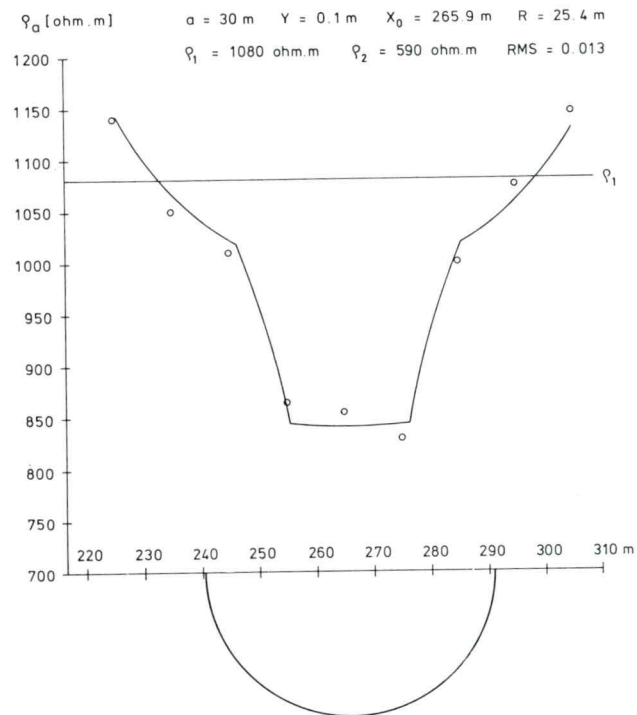


Fig. 63. Location 20, profile P-11, $a = 30$ m. Observed and best fit hemisphere model data

Sl. 63. Lokacija 20, profil P-11, $a = 30$ m. Rezultat numerične obdelave anomalije z modelom polkrogle

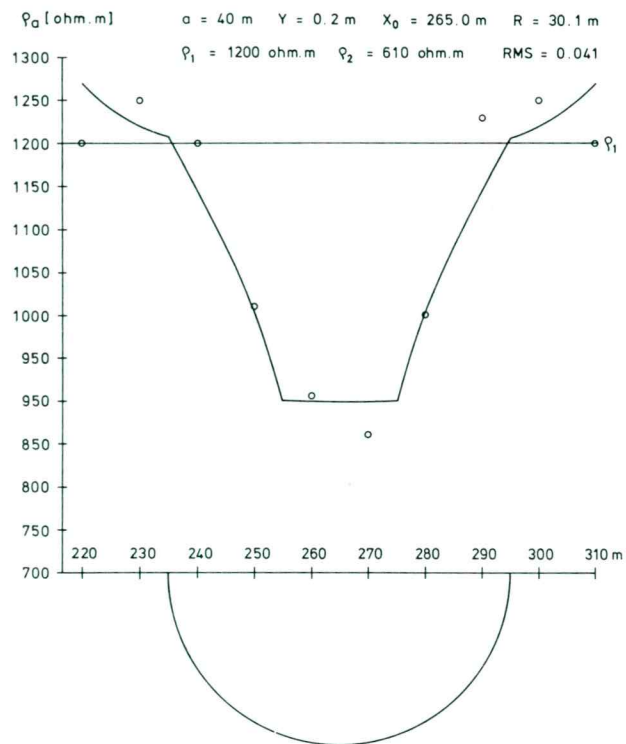


Fig. 64. Location 20, profile P-11, $a = 40$ m. Observed and best fit hemisphere model data

Sl. 64. Lokacija 20, profil P-11, $a = 40$ m. Rezultat numerične obdelave anomalije z modelom polkrogle

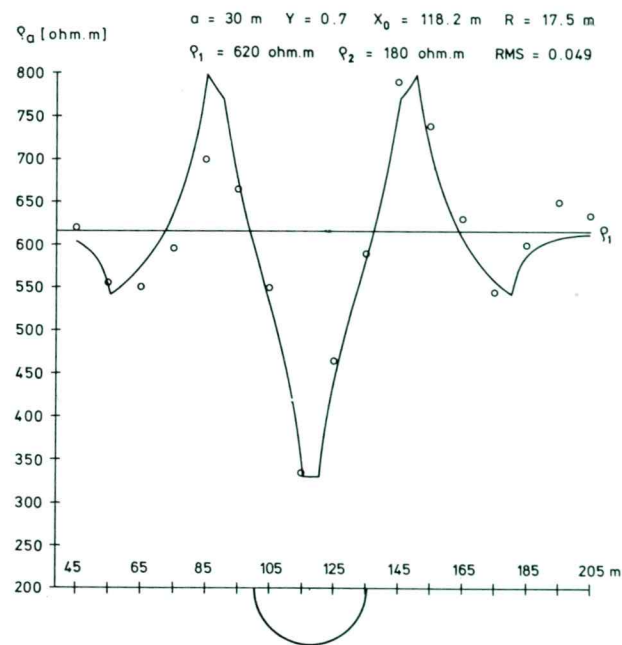


Fig. 65. Location 26, profile P-15 a. Observed and best fit hemisphere model data

Sl. 65. Lokacija 26, profil P-15 a. Rezultat numerične obdelave anomalije z modelom polkrogle

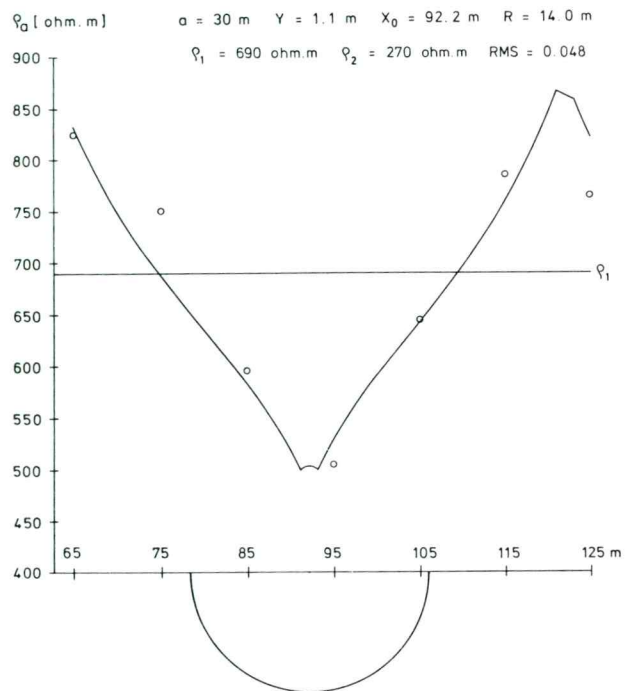


Fig. 66. Location 61, profile P-33 a. Observed and best fit hemisphere model data

Sl. 66. Lokacija 61, profil P-33 a. Rezultat numerične obdelave anomalije z modelom polkrogle

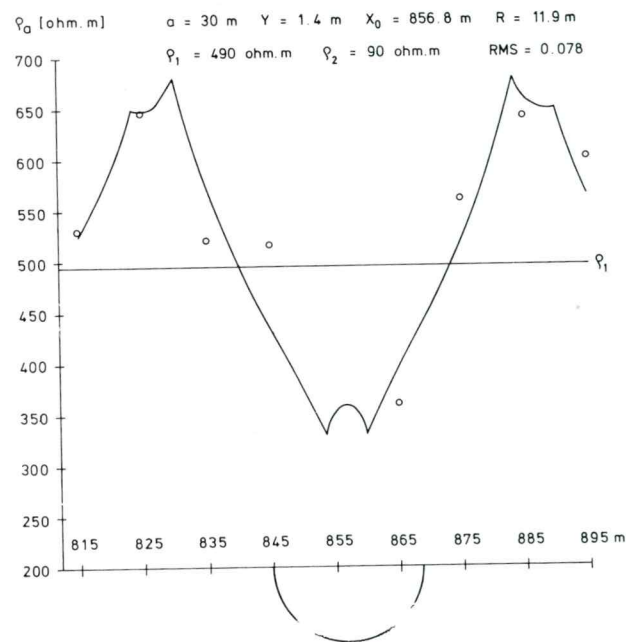


Fig. 67. Location 105, profile P-56. Observed and best fit hemisphere model data

Sl. 67. Lokacija 105, profil P-56. Rezultat numerične obdelave anomalije z modelom polkrogle

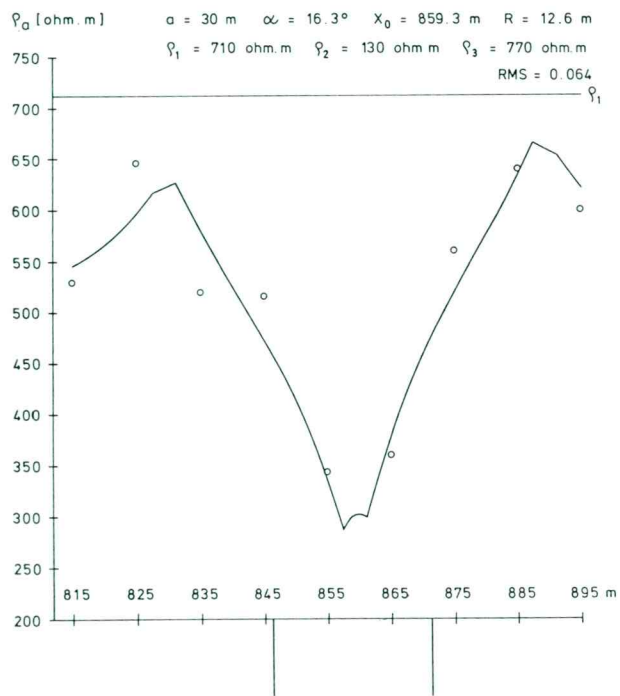


Fig. 68. Location 105, profile P-56. Observed and best fit vertical dike model data

Sl. 68. Lokacija 105, profil P-56. Rezultat numerične obdelave anomalije z modelom vertikalne plošče

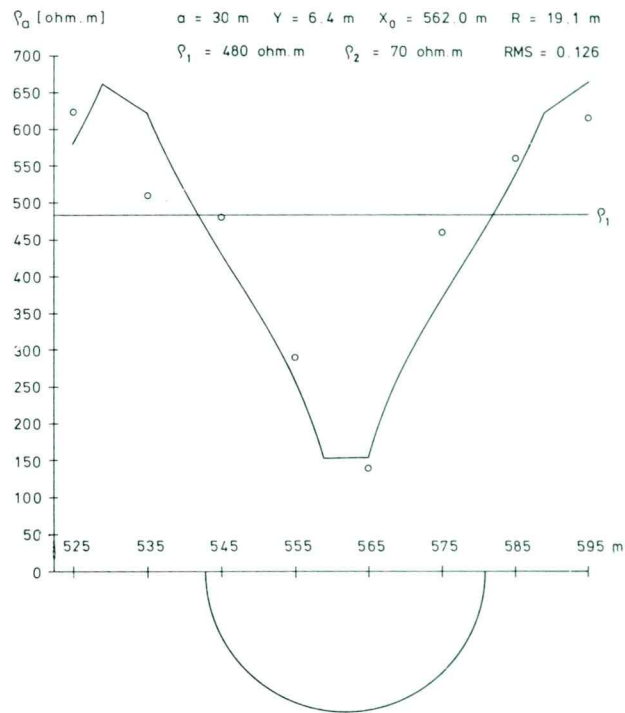


Fig. 69. Location 109, profile P-69. Observed and best fit hemisphere model data

Sl. 69. Lokacija 109, profil P-69. Rezultat numerične obdelave anomalije z modelom polkrogle

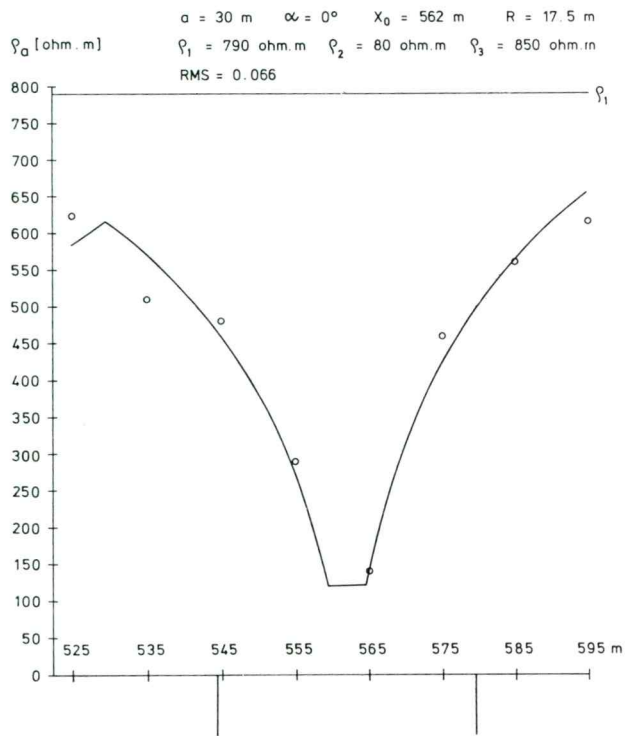


Fig. 70. Location 109, profile P-69. Observed and best fit vertical dike model data

Sl. 70. Lokacija 109, profil P-69. Rezultat numerične obdelave anomalije z modelom vertikalne plošče

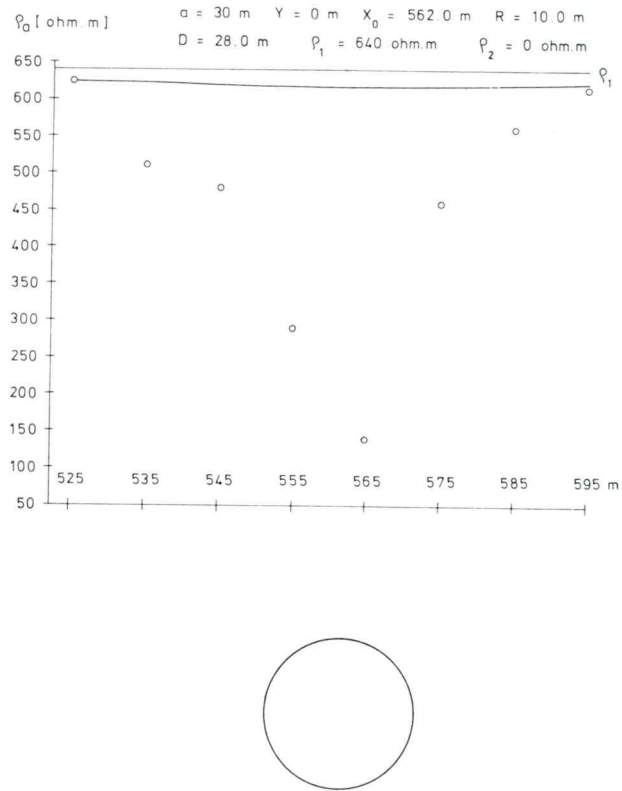


Fig. 71. Location 109, profile P-69. Observed data and theoretical plot over direct model — hemisphere in homogeneous halfspace

Sl. 71. Lokacija 109, profil P-69. Rezultat numerične obdelave anomalije z neposrednim modelom — kroglja v homogenem polprostoru

3.3. Discussion

A quantitative interpretation of resistivity anomalies of the Istrian bauxite deposits shows that the anomalies may only be explained by models of surface bodies. Comparatively simple models, like the hemisphere and the dike, make it possible to process a satisfactory quantitative anomaly by means of desk-computers like, for example, the Hewlett Packard 9830 A. For practical purposes, it is necessary to define the position and the approximate limits of the plate-shaped depressions superposed above the bauxite, which the above mentioned models do. The evaluation of such geometrical parameters may be quite adequately done without special calculation. It is clear, however, that more reliable qualitative information may be obtained by numerical processing.

Model investigations have given the answer to some questions raised in the field work. Firstly the choice of the Wenner array has been justified by the model curve analysis, as far as the simplicity of processing is concerned. And secondly, the suitability of anomaly elimination was likewise justified for locations where the thickness of terra rossa and clay fillings is relatively small. In addition to this, the quantitative processing results answer some other questions. Referring to the discovered bauxite deposits, the selection of the array spacing proved to be appropriate. The ratio of the array spacing versus the size of settlement, is in most cases closely approaching the optimum.

However, limitation to one single array spacing is likely to provoke suspicion that some bauxite deposits with less favourable settlement dimensions (the radius being far from 30 m, for which the array of $a = 30$ m, is most sensitive) do not respond with adequate anomalies, or that because of their low values, they can be overlooked. It is advantageous to operate with variable spacing between the electrodes, since a greater number of array dimensions certainly provides more information. However, in the attempt to justify the application of merely one array dimension, it is possible to find some arguments, other than financial. The applied array is sufficiently sensitive in the case of larger subsidences, since the depth of investigation is less important. Besides, larger subsidences may or may not be indicative of deeper bauxite bodies representing unfavorable mining propositions. On the other hand, settlements of limited size very likely harbour small bauxite bodies.

Numerical processing entirely confirms the qualitative interpretation of apparent resistivity anomalies and the corresponding explanation of the cause of anomalies.

4. Conclusions

The resistivity survey is applicable for the exploration of covered geological structures, such as ore bodies. The applicability of the resistivity survey, however, is limited to minor depths. The bauxite pockets within the Istrian Cretaceous limestone, for instance, lie far too deep to affect the electrical field on the surface to a significant extent. Although the resistivity of bauxite is several times lower than that of the surrounding limestone, it cannot be detected directly. In spite of this, the Istrian bauxite deposits are clearly evident in the apparent resistivity anomalies which are related to their hanging wall of Eocene limestone. Overlying the bauxite pocket, the wet fissured limestone

layer responds as a low resistivity body. The model of the hemispheroid is applicable to such geological structures and, in the extreme, the model of the vertical dike can be considered as well. The comparison of observed resistivity anomaly curves of bauxite pockets with model curves pertaining to both types show that the geological structure can be satisfactorily illustrated by the two models, notwithstanding the impression of a very rough approximation. Theoretical anomalies obtained by computer data processing differ from the corresponding observed anomalies at an average of only a few percent. This equivalence does certainly not imply that the models correspond so closely to the geological structure.

In this article, besides the qualitative and quantitative interpretations of apparent resistivity anomalies of the Istrian bauxite deposits, there is a collection of hemisphere resistivity type curves and some curves pertaining to the vertical dike. In the case of the conductive hemispheroid, an interesting paradox emerged: the thinner the hemispheroid, the higher the anomaly.

References

- Cook K. L., Gray R. L., 1961, Theoretical horizontal resistivity profiles over hemispherical sinks. *Geophysics* 26, 342—354.
- Cook K. L., Van Nostrand R. G., 1954, Interpretation of resistivity data over filled sinks. *Geophysics* 19, 761—790.
- Hmelevskoj V. K., 1970, Osnovnoj kurs elektrorazvedki, čast I, Elektrorazvedka postojannim tokom. Izdatelstvo Moskovskogo Universiteta.
- Jain Sh. C., 1974, Theoretical broadside resistivity profiles over an outcropping dike. *Geophys. Prosp.* 22, 445—457.
- Krulc Z., Vidović N., 1960, Primjena metode otpora kod istraživanja boksitnih ležišta pod pokrovom u Istri. *Vesnik, knjiga I, Serija C, Beograd.*
- Kumar Rakesh, 1973, Resistivity type curves over outcropping vertical dyke — I. *Geophys. Prosp.* 21, 560—578.
- Kumar Rakesh, 1973, Resistivity type curves over outcropping vertical dyke — II. *Geophys. Prosp.* 21, 615—625.
- Lapajne J., 1969, Geoelektrične raziskave boksitnih nahajališč. *Geologija* 12, 153—159, Ljubljana.
- Lapajne J., 1974, Geofizikalne raziskave na krasu. *Acta carsologica* VI, 397 do 420, Ljubljana.
- Lapajne J., 1968, Influence of the Low Resistivity Surface Layer in Geoelectric Mining Prospecting. *Mining and Metallurgy Quarterly*, No. 3, 29—34, Ljubljana.
- Lapajne J., 1975, Some Remarks about the Geophysical Exploration of the Karst. *Proceedings of the 6th International Congress of Speleology — Olomouc 1973, I.*, 291—295, Praha.
- Lapajne J., 1976, Some Remarks about the Geoelectrical Exploration of Buried Bodies. *Geologija* 19, 275—285, Ljubljana.
- Matveev B. K., 1961, Električeskoe pole točečnogo istočnika v mnogoslojnoj srede s šarovim vključenjem. *Izvest. Akad. nauk SSSR, Ser. Geofiz.*, No. 12, 1784—1791.
- Van Nostrand R. G., 1953, Limitations on resistivity methods as inferred from the buried sphere problem. *Geophysics* 18, 423—433.